Unmasking the history of 3C 293 with LOFAR sub-arcsecond imaging ⋆

Pranav Kukreti[1,2]⋆⋆, Raffaella Morganti[2,1], Timothy W. Shimwell[2,3], Leah K. Morabito[4,5], Robert J. Beswick[6], Marisa Brienza[7,8], Martin J. Hardcastle[9], Frits Sweijen[3], Neal Jackson[6], George K. Miley[3], Javier Moldon[10], Tom Oosterloo[2,1], Francesco de Gasperin[11,8]

[1] Kapteyn Astronomical Institute, University of Groningen, Postbus 800, 9700 AV Groningen, The Netherlands
[2] ASTRON, the Netherlands Institute for Radio Astronomy, Oude Hoogeveensedijk 4, 7991 PD Dwingeloo, The Netherlands
[3] Leiden Observatory, Leiden University, P.O.Box 9513, NL-2300 RA, Leiden, The Netherlands
[4] Centre for Extragalactic Astronomy, Department of Physics, Durham University, Durham DH1 3LE, UK
[5] Institute for Computational Cosmology, Department of Physics, University of Durham, South Road, Durham DH1 3LE, UK
[6] Jodrell Bank Centre for Astrophysics, School of Physics and Astronomy, University of Manchester, Oxford Rd, Manchester M13 9PL,UK
[7] Dipartimento di Fisica e Astronomia, Università di Bologna, via P. Gobetti 93/2, 40129, Bologna, Italy
[8] INAF - Istituto di Radioastronomia, Via P. Gobetti 101, 40129, Bologna, Italy
[9] Centre for Astrophysics Research, University of Hertfordshire, College Lane, Hatfield AL10 9AB, UK
[10] Instituto de Astrofísica de Andalucía (IAA, CSIC), Glorieta de las Astronomía, s/n, E-18008 Granada, Spain
[11] Hamburger Sternwarte, Universität Hamburg, Gojenbergsweg 112, D-21029, Hamburg, Germany July 21, 2021

July 21, 2021

ABSTRACT

Active galactic nuclei (AGNs) show episodic activity, which can be evident in galaxies that exhibit restarted radio jets. These restarted jets can interact with their environment, leaving signatures on the radio spectral energy distribution. Tracing these signatures is a powerful way to explore the life of radio galaxies. This requires resolved spectral index measurements over a broad frequency range including low frequencies. We present such a study for the radio galaxy 3C 293, which has long been thought to be a restarted galaxy on the basis of its radio morphology. Using the International LOFAR telescope (ILT) we probed spatial scales as fine as ~0.2″at 144 MHz, and to constrain the spectrum we combined these data with Multi-Element Radio Linked Interferometer Network (MERLIN) and Very Large Array (VLA) archival data at frequencies up to 8.4 GHz that have a comparable resolution. In the inner lobes (~2 kpc), we detect the presence of a spectral turnover that peaks at ~225 MHz and is most likely caused by free-free absorption from the rich surrounding medium. We confirm that these inner lobes are part of a jet-dominated young radio source (spectral age $\lesssim$0.17 Myr), which is strongly interacting with the rich interstellar medium (ISM) of the host galaxy. The diffuse emission surrounding these lobes on scales of up to ~4.5 kpc shows steeper spectral indices ($\Delta\alpha \sim$ 0.2-0.5, S $\propto \nu^{-\alpha}$) and a spectral age of $\lesssim$0.27 Myr. The outer lobes (extending up to ~100 kpc) have a spectral index of $\alpha \sim$ 0.6-0.8 from 144-4850 MHz with a remarkably uniform spatial distribution and only mild spectral curvature ($\Delta\alpha \lesssim$ 0.2). We propose that intermittent fuelling and jet flow disruptions are powering the mechanisms that keep the spectral index in the outer lobes from steepening and maintain the spatial uniformity of the spectral index. Overall, it appears that 3C 293 has gone through multiple (two to three) epochs of activity. This study adds 3C 293 to the new sub-group of restarted galaxies with short interruption time periods. This is the first time a spatially resolved study has been performed that simultaneously studies a young source as well as the older outer lobes at such low frequencies. This illustrates the potential of the International LOFAR telescope to expand such studies to a larger sample of radio galaxies.

Key words. galaxies: active – radio continuum: galaxies – galaxies: individual: 3C 293 - techniques: high angular resolution

1. Introduction

Over the past decades, active galactic nuclei (AGNs) have been demonstrated to show episodic activity and have been identified in different phases of their life cycle. Lobes of remnant plasma from a previous phase of activity coexisting with a newly born pair of radio jets are typical indicators of restarted or episodic activity in such galaxies (for a review, see Saikia & Jamrozy 2009). Restarted radio galaxies have been used to constrain the timescales of activity and quiescence (and therefore the duty cy-

cle), which are crucial to understand the life cycle of these galaxies (Morganti 2017).

The life cycle of a radio galaxy is understood to start from a phase of morphologically compact radio emission with an absorbed or steep spectrum. Such sources are called compact steep spectrum (CSS) and gigahertz peaked spectrum (GPS) sources (O'Dea 1998; Fanti 2009; O'Dea & Saikia 2021). These sources show morphological similarities to large-scale radio sources, but with sizes of just a few kiloparsecs (similar to galactic scales), and they are thought to develop into large-scale radio galaxies. However, intermittent AGN activity may prevent some of these types of sources from growing to large-scale radio galaxies.

After an initial phase of activity that can last between ~10^7 yr and ~10^8 yr (Parma et al. 1999, 2007; Hardcastle 2018), the nu-

---

clear activity stops and the injection of fresh plasma to the lobes ceases. In some cases, the cessation of activity can lead to observable remnant plasma lobes without any activity near the core (Parma et al. 2007; Murgia et al. 2010). These lobes are heavily affected by radiative losses that causes spectral steepening. This remnant phase has been detected in a small fraction (<10%) of radio galaxies (Saripalli et al. 2012; Brienza et al. 2017; Mahatma et al. 2018; Quici et al. 2021). A slightly more frequently observed (13-15% of radio galaxies; Jurlin et al. 2020) scenario is one where the activity is intermittent and radio plasma from an older phase as well as radio jets from a newer phase are simultaneously visible suggesting that activity has restarted after a relatively short remnant phase (Schoenmakers et al. 1998; Stanghellini et al. 2005; Shulevski et al. 2012). Indeed, the results from the growing statistics of radio galaxies in less common phases, such as remnants and restarted galaxies, combined with new modelling confirm not only the presence of a life cycle of activity, but also favour a power-law distribution for the ages, which implies a high fraction of short-lived AGNs (see Shabala et al. 2020; Morganti et al. 2020).

Restarted radio galaxies provide a unique opportunity to observe and subsequently model the spectral and morphological properties of the older and newer lobes simultaneously. The characterisation of these properties can be used to estimate ages and timescales of their period of activity.

Identifying restarted galaxies is not easy as they can show a variety of properties depending on the radio galaxy itself. A well known group of restarted galaxies are the double-double radio galaxies (DDRGs; Schoenmakers et al. 2000) in which a new pair of radio lobes are seen closer to the nucleus than the older lobes. Restarted galaxies with three pairs of radio lobes have also been identified, the so-called 'triple-double' galaxies, for example B 0925+420 (Brocksopp et al. 2007), 'Speca' (Hota et al. 2011) and J 1216+0709 (Singh et al. 2016). In the case of DDRGs, spectral age studies have provided estimates of the timescale of the quiescent phase to be between 10^5 yr and 10^7 yr and at most, ∼50% of the length of the previous active phase (Konar et al. 2013; Orru et al. 2015; Nandi et al. 2019; Marecki et al. 2020; Marecki 2021).

DDRGs represent only a fraction of restarted galaxies and in other cases, compact inner jets are found embedded in low-surface brightness, large-scale lobes (Jamrozy et al. 2009; Kuźmicz et al. 2017) or a relatively bright core (Jurlin et al. 2020). However, it is not always possible to identify restarted galaxies based on morphology alone. Over the years, spectral properties of radio galaxies have also been used to identify restarted radio galaxies (Parma et al. 2007; Murgia et al. 2010; Jurlin et al. 2020; Morganti et al. 2020). One such interesting case is of 3C 388, where a dichotomy in the spectral index distribution between different regions of the lobes was found which indicated two different jet episodes (Burns et al. 1982; Roettiger et al. 1994). More recently, Brienza et al. 2020 used the LOw Frequency Array (LOFAR) (van Haarlem et al. 2013) to confirm the presence of restarted activity in this galaxy. Jurlin et al. (2020) used the presence of a steep spectrum core ($\alpha_{1360\,\mathrm{MHz}}^{150\,\mathrm{MHz}} > 0.7$, where $S_\nu \propto \nu^{-\alpha}$), along with morphological properties such as low surface brightness extended emission to identify candidate restarted galaxies.

Over the past few years, a new sub-group of candidate restarted radio galaxies has been found, which do not show spatially resolved spectral properties expected from old remnant plasma, for example an ultra steep spectrum ($\alpha > 1.2$) and a steep curvature in the radio spectra ($\Delta\alpha \geq 0.5$). Instead, these sources show bright inner jets and very diffuse outer lobes with a

homogeneous spatial distribution of spectral index, for example Centaurus A (McKinley et al. 2018, 2013; Morganti et al. 1999), B2 0258+35 (Brienza et al. 2018), and more recently NGC 3998 (Sridhar et al. 2020). Although the physical mechanism responsible for these properties is still under debate, some studies indicate that the older outer lobes could still be fuelled at low levels by the active inner jets (McKinley et al. 2018). This is different from the model of typical restarted galaxies where fuelling of the older lobes has stopped. Therefore, this sub-group poses a new challenge to our understanding of the life-cycle of radio galaxies.

Characterising the spectral properties of restarted galaxies is challenging, because it requires a wide frequency coverage to frequencies above 1.4 GHz to include the high frequency end, where the effects of radiative losses are dominant due to ageing and cessation of fuelling, and down to a few tens/hundreds of MHz, where the signatures of plasma injection are alive for the longest time. One way to study such galaxies is to use the International LOFAR Telescope (ILT) which allows us to resolve the emission from such galaxies at arcsecond resolution down to low frequencies (144 MHz), and complement observations at GHz frequencies. The LOFAR telescope includes 13 international stations, providing baselines of up to 1989 km which translates to an angular resolution of 0.27″ at 150 MHz. Although these international stations have always been available, there have only been a handful of sub-arcsecond studies with the telescope (Moldón et al. 2014; Jackson et al. 2016; Morabito et al. 2016; Varenius et al. 2015, 2016; Ramírez-Olivencia et al. 2018; Harris et al. 2019; Kappes et al. 2019). This is mainly due to the fact that the calibration with the full international LOFAR telescope is technically challenging. However, with the development of a new calibration strategy, presented in detail in **?**, it is now possible to more routinely perform high resolution low frequency studies of these galaxies. We can make use of this capability to search for the presence of a newer phase of activity in restarted radio galaxies and study the properties of small-scale (a few kpc) emission down to MHz frequencies. Combined with the Dutch stations of LOFAR, we can also study the large-scale emission (hundreds of kpc) from these galaxies.

This paper is structured in the following manner: In Sect. 1, we give an introduction to the source, in Sect. 2, we describe the data and the data reduction procedures, and the procedure to make spectral index maps; in Sect. 3 we present the large and small-scale source morphology, the large and small-scale spectral index, large-scale spectral age analysis, and the absorption models for the inner lobes in the centre. In Sect. 4, we discuss the properties and results for the central region and the outer lobes and then summarise the evolutionary history of 3C 293. Throughout the paper, we define the spectral index α, was calculated using the convention: $S \propto \nu^{-\alpha}$. The cosmology adopted in this work assumes a flat universe with $H_0 = 71$ km s^{-1} Mpc^{-1}, $\Omega_\mathrm{m} = 0.27$ and $\Omega_\mathrm{vac} = 0.73$. At the redshift of 3C 293, 1″ corresponds to 0.873 kpc.

2. Overview of the source 3C 293

3C 293 is a nearby radio galaxy at a redshift of $z = 0.045$ (de Vaucouleurs et al. 1991). The large and small-scale structure of 3C 293 has been studied before in the radio and has a number of peculiarities. When observed at arcsec-resolution the source shows two asymmetric radio lobes and a central compact component (Figure 1a) and a total extension of ∼220 kpc. Bridle et al. (1981) were the first to study the asymmetric large-scale outer lobes that have bright concentrations of emission at their further
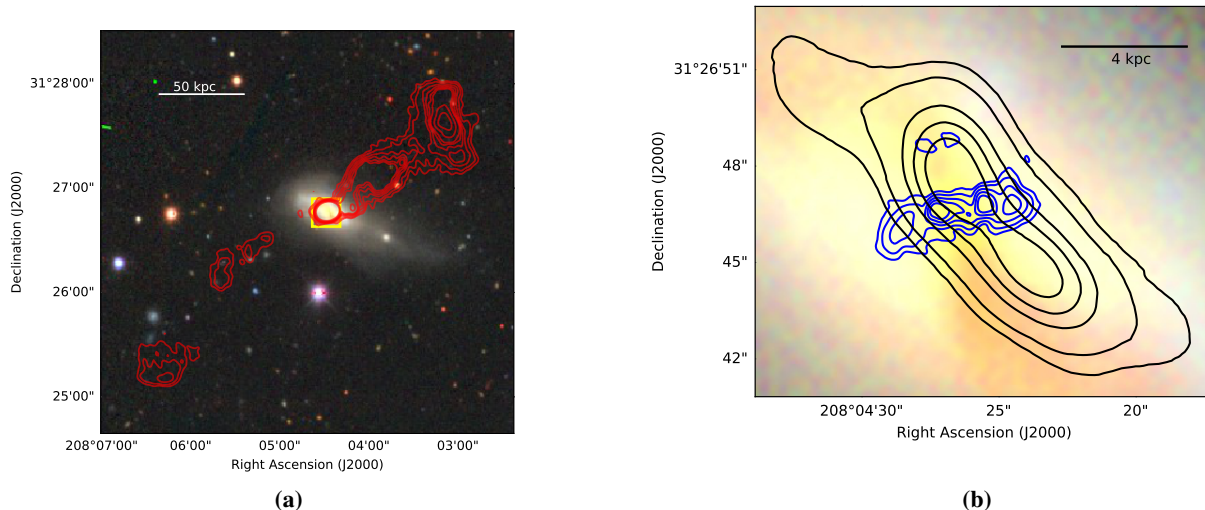
(a)

(b)

Figure 1: (a) RGB colour image of the host galaxy of 3C 293 from DECaLS[1] (Dey et al. 2019). A small companion galaxy can be seen in the south-west, ~37″ away from the host galaxy. The red contours show the Very Large Array (VLA) 1.36 GHz emission at 4.6″×4.1″ resolution from archival data we have reprocessed. The outer lobes extend in the north-west and south-east direction and are aligned almost perpendicular to the orientation of the dust lanes and the gas disk. The blue box marks the region covered by the blue contours in the right panel. (b) DECaLS RGB colour image overlaid with black contours that map the CO(1-0) emission disc from Labiano et al. (2014) with the south-western side approaching us and northeastern side receding. The blue contours show the 120-168 MHz radio continuum emission from the inner ~4.5 kpc as seen in our new LOFAR image. The inner lobes extend in east and west and can be seen to bend out of the host galaxy's CO disk, especially in the east.

points from the core. A total luminosity of L(1.4 GHz) = 2×10²⁵ W Hz⁻¹ places 3C 293 on the border of the FR-I/FR-II classification (Fanaroff & Riley 1974). The bright steep-spectrum centre and presence of large and small-scale lobes have been used to identify 3C 293 as a candidate for restarted activity (Bridle et al. 1981; Akujor et al. 1996).

Sub-arcsecond resolution studies have resolved the ~4.5 kpc central region, shown in Figure 1b. Two prominent peaks of emission, understood to be the inner lobes, were found embedded in diffuse emission (Akujor et al. 1996; Beswick et al. 2002, 2004). There is an abrupt drop in the surface brightness of the outer lobes, which is ~2500 times lower compared to the diffuse emission in the centre. Beswick et al. (2004) and Floyd et al. (2005) concluded that the eastern lobe is approaching us and the western lobe is receding. This picture of the orientation was also suggested by Mahony et al. (2016) (see their Figure 7) who studied the ionised gas outflows in the inner few kpc. One of the most striking features of the radio morphology of the galaxy is the ~35° (projected) misalignment between the inner and outer lobes, the origin of which is still unclear, although Bridle et al. (1981) suggested that the misalignment could be explained by radio jet refraction due to pressure gradients in dense circumgalactic atmospheres. More recently, Machalski et al. (2016) concluded that a fast realignment of the jet axis, resulting from a rapid flip of the black hole spin, could be responsible for this misalignment. Such misalignment is rare in radio galaxies.

Joshi et al. (2011) performed an integrated spectral index study of the source covering a frequency range of 154 MHz to 4860 MHz by using the Giant Metrewave Radio Telescope (GMRT) and the VLA and estimated spectral ages. They obtained a straight spectrum for several regions of the source with a spectral index of α_{4860}^{154} = 0.72±0.02, 0.80±0.02 and 0.91±0.03 for the central region, outer north-western lobe and outer south-eastern lobe, respectively. Assuming an equipartition magnetic field and a break frequency equal to the highest frequency of

their observations, they derived a spectral age of ≤16.9 Myr and ≤23 Myr for the north-western and south-eastern lobes respectively. Using a jet speed of c and a hotspot lifetime of ~ 10⁴ − 10⁵ yr, they estimated a time period of ~ 0.1Myr for the interruption of activity. Since the real jet speed will be lower than c (≲0.3-0.6c; Arshakian & Longair 2004; Jetha et al. 2006), the actual interruption time period is of course, higher. They argue that within this time the inner double must also form. However, the integrated spectral index measurements for the outer lobes can not give any information about the spectral properties of plasma as a function of distance from the centre, needed to understand the physical processes active in the lobe. Detailed resolved studies are required for this purpose.

From studies at other wavelengths we know that 3C 293 is hosted by a peculiar elliptical galaxy VV5-33-12 showing multiple dust lanes and compact knots (van Breugel et al. 1984; Martel et al. 1999; de Koff et al. 2000; Capetti 2000). An RGB colour image of the host galaxy is shown in Figure 1. The host galaxy is a post-coalescent merger that is undergoing a minor interaction with a close satellite galaxy that lies to ~37″ towards the south-west (Emonts et al. 2016). Emonts et al. 2016 suggest that the merger in 3C 293 may provide the fuel to trigger the AGN activity. Large amounts of gas (M(cold H₂) = 2.3×10¹⁰ M⊙ = 3.7×10⁹ M⊙) have also been found in both emission and absorption in the central few kiloparsecs (Evans et al. 1999, 2005; Ogle et al. 2010) confirming the presence of a dense ISM. Labiano et al. (2014) find that the molecular gas (traced by CO(1-0)) is distributed along a 21 kpc diameter warped disk, that rotates around the AGN (Figure 1b).

3. Observations and data reduction

In order to trace the radio emission and characterise the spectral properties over a broad range of frequencies and on large and small scales, we used data from different telescopes. We
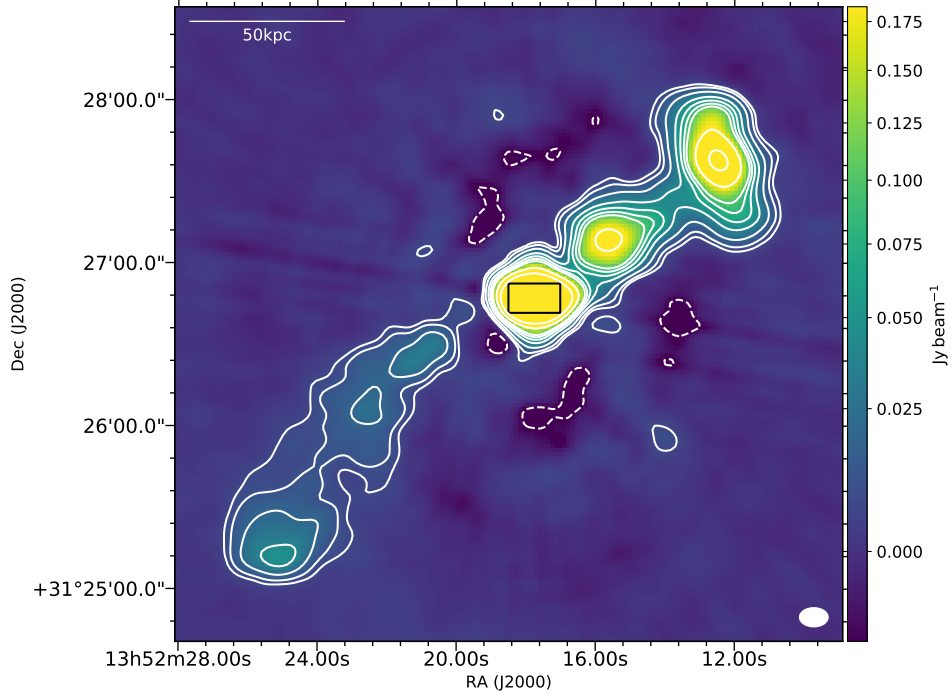
(a) Dutch array
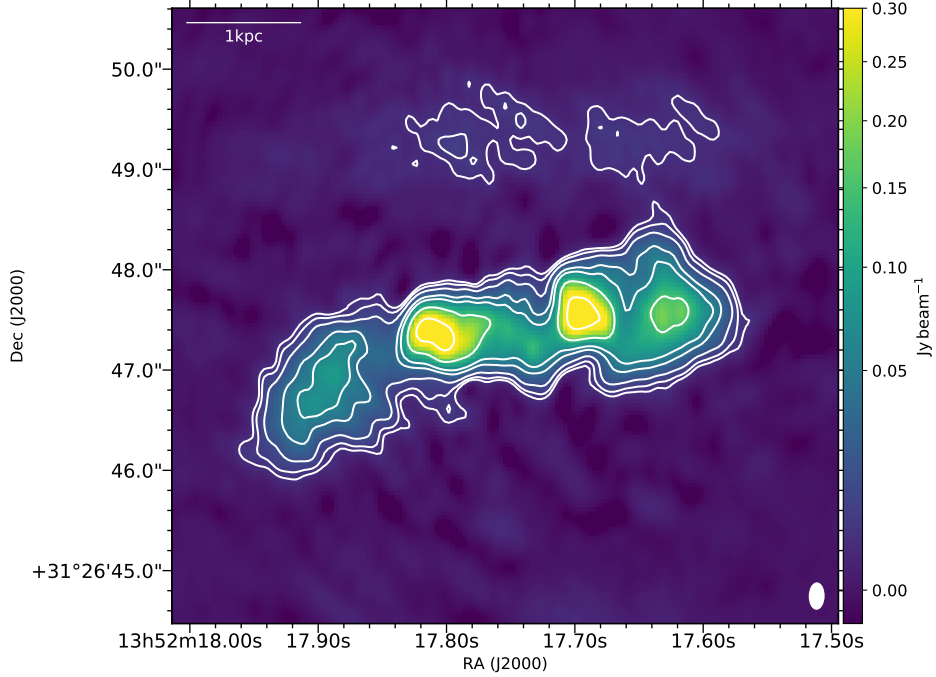
(b) International array

Figure 2: (a) LOFAR HBA image with Dutch array from LoTSS-DR2 data showing the large-scale ($\sim$250$''$) structure in 3C 293 at 144 MHz with a resolution of $10.5'' \times 7''$. The contours marking the large-scale structure are at: (-3, 3, 5, 10, 20, 30, 40, 50, 100, 200)$\times \sigma_{RMS}$ where σ_{RMS} = 2 mJy beam^{-1} is the RMS noise in the image. The black rectangle in the centre marks the region that is shown in the high resolution image. (b) The LOFAR HBA image with international stations at 144 MHz of the central 4.5 kpc region with a resolution of $0.26'' \times 0.15''$. The small-scale inner lobes and diffuse emission are visible and are marked with contours at: (-3, 3, 5, 10, 25, 40, 100, 250)$\times \sigma_{RMS}$ where σ_{RMS} = 1.5 mJy beam^{-1} is the RMS noise in the image. Image statistics for all images are summarised in Table 2

Table 1: Summary of LOFAR observations.

Configuration	Central frequency (MHz)	Bandwidth (MHz)	TOS[1] (hours)	Interval[2] (seconds)	Calibrators	Observation date
HBA Dutch[3]	144	48	8	1	3C196, 3C295	12 April 2018
HBA International	144	48	4+4	1	3C295	30 July and 02 August 2020

[1] Time on source for the target, [2] Sample integration interval (time resolution of the data), [3] HBA Dutch array data from LoTSS-DR2

use new observations with the ILT High Band Antenna (HBA) at 120-168 MHz. We combine these with archival VLA data at 1.36 GHz and 4.85 GHz for a low resolution spectral study. For the high resolution complementary data, we use archival Multi-Element Radio Linked Interferometer Network (MER-LIN) 1.36 GHz, VLA 4.85 GHz and 8.45 GHz data.

3.1. LOFAR HBA observations

We performed targeted observations of 3C 293 with the ILT HBA for a total of 8 hours split into two 4 hour observing runs, on 30 July 2020 and 02 August 2020 (Project code - LC14_015). The 60 Dutch stations and 12 international stations were used as a part of the ILT array. The international stations used for the observations were - DE601, DE602, DE603, DE604, DE605, FR606, SE607, UK608, DE609, PL610, PL612 and IE613. The observations were carried out with the standard survey setup (Shimwell et al. 2019), with a 48 MHz bandwidth centred at 144 MHz. The bandwidth was split into channels of 12.2 KHz width with an integration time of 1s. 3C 295 and 3C 196 were used as the flux density calibrators and observed for 10 mins before and after each target observation. After observing, the data was passed through the standard LOFAR pre-processing pipeline (Heald et al. 2010) where the RFI flagging (AOFlagger; Offringa et al. 2010, 2012) and averaging down to 1 second per sample and 4 channels per subband, was carried out. The processed measurement sets were then passed through the PREF-ACTOR[2] pipeline (de Gasperin et al. 2019; van Weeren et al. 2016; Williams et al. 2016) with the default parameter settings for direction independent calibration. A high resolution model of 3C 295 was used for calibration. Stations RS509 and PL610 were flagged for the 02 August data set due to bad data.

The data from the Dutch and international array have to be reduced using different procedures. This is due to fact that the international stations have different clocks and beams than the core and remote stations of ILT. Also, at low frequencies, the ionospheric effects become immensely relevant where they play an important role in corrupting astronomical signals (Intema et al. 2009). The wide geographical spread of the ILT means that different international stations see through very different regions of atmosphere. The data reduction procedures are described in the next two subsections.

3.1.1. High resolution LOFAR International array

The processed data from the PREFACTOR pipeline, including the international stations, were averaged and calibrated using the LOFAR long baseline pipeline[3] (Morabito et al. 2021), which performs in-field delay calibration using a bright calibrator in the field of view and cross-matching it with the LOFAR Long-Baseline Calibrator Survey (Jackson et al. 2016, 2021) and LO-

---

FAR Two-metre Sky Survey (LoTSS) (Shimwell et al. 2017). The pipeline first averages the data to a resolution of 8s in time and 97.64 KHz in frequency, that is two channels per subband. It then performs dispersive delay calibration using the in-field delay calibrator close to the target, which in our case was L465974 (J2000.0 RA $13^h53^m11.69^s$, Dec. $+32°05'42.6''$), located at an angular distance of $0.7°$ from the target. The two 4 hr data sets were processed separately and were combined after applying their respective delay calibration solutions. The combined 8 hr data set was then used for self-calibration and imaging of the delay calibrator using the procedure outlined in van Weeren et al. (2020) which makes use of WSClean (Offringa et al. 2014; Offringa & Smirnov 2017) for imaging. We estimated an integrated flux density of 0.78 Jy for the delay calibrator, which is within 10% of the integrated flux density of 0.85 Jy from LoTSS-DR2. This gives us confidence in our flux scale.

The dispersive delay calibrator solutions were then transferred to the target separately for each 4 hr data set. Rounds of self-calibration and imaging were performed on the combined calibrated target data set using the same procedure with a Briggs weighting scheme and a robust of -1 which gave a synthesised beamwidth of $0.26''\times0.15''$. We measure an integrated flux density of 10.04 ± 1.01 Jy for the target, which is in good agreement with the integrated flux density of the central region which is 10.70 ± 1.07 Jy (see region C in Table 3). The RMS noise in the final map is ~0.2 mJy beam^{-1}which increases up to ~1.5 mJy beam^{-1}near the target. The thermal noise for the image is 0.08-0.1 mJy beam^{-1}and the noise level in our image is dominated presumably by residual phase and amplitude errors around a bright source. We have used a flux scale error of 10% and the final high resolution map is shown in Figure 2b.

3.1.2. LOFAR Dutch array and LoTSS-DR2 resolution

The quality of the low resolution image made with only the Dutch array of the targeted observations was not good enough to perform a spectral analysis, compared to a similar resolution image made with a LoTSS-DR2 (Shimwell et al. in prep) pointing. Hence its data reduction process is not discussed further.

We have instead used the Dutch array data from a LoTSS-DR2 pointing with the reference code P207+32 (Project code - LC7_024) for the low resolution image. In this pointing, the target lies $1.2°$ away from the phase centre. The observations were carried out using the standard survey setup, that is 8 hours on-source time, 48 MHz bandwidth centred at 144 MHz divided over 231 subbands, and 1 second integration time. The Dutch array data are averaged to 8s in time and 2 channels per 1.95 MHz subband. The flux density calibrator was 3C 196. Although the observations were carried out with the entire LOFAR array (Dutch array and international stations), we only use the data from the Dutch array here to image the large-scale structure. We did not use this international stations data for the high resolution image because the target was too far from the phase centre

---

[2] https://github.com/lofar-astron/prefactor
[3] https://github.com/lmorabit/lofar-vlbi

Table 2: Image statistics summary.

Frequency (MHz)	Telescope	Resolution (BPA) ('')	RMS noise (mJy beam^{-1})	Integrated flux density ± error (Jy)
144	LOFAR HBA Dutch	10.5''×7''(90°)	2.0	15.19±1.52
1360	VLA B configuration	4.6''×4.1''(74°)	0.08	4.68±0.23
4850	VLA C configuration	6.0''×6.0''(90°)	0.22	1.88±0.09
144	LOFAR HBA international	0.26''×0.15''(1°)	1.5	10.04±1.01
1360	MERLIN	0.24''×0.21''(33°)	1.2	3.72±0.19
4850	VLA C configuration	0.36''×0.30''(53°)	0.2	1.49±0.07
8450	VLA C configuration	0.30''×0.26''(70°)	0.26	1.01±0.05

The first three rows show measurements of the entire ~200 kpc source (centre+outer lobes) from the low resolution images. The last four rows show measurements from the high resolution image of the ~4.5 kpc centre.

for high fidelity high resolution imaging. The data were processed using the direction dependent self-calibration pipeline, DDF-pipeline[4], described in detail in Shimwell et al. (2019); Tasse et al. (2020). The flux scale is consistent with LoTSS-DR2. LoTSS-DR2 is scaled to Roger et al. (1973) flux scale (consistent with Scaife & Heald 2012) through statistically aligning to the 6C survey assuming a global NVSS/6C spectral index.

To improve image quality, the target was extracted from the self-calibrated data after subtracting from the uv-data, all the sources located in the field of view other than 3C 293 (and a few other sources nearby). Additional self-calibration and imaging loops were then performed on the extracted data set (van Weeren et al. 2020) using WSClean for imaging and NDPPP for calibration. The final image has a beam size of 10.5''×7''and has an off-source RMS of 0.3mJy beam^{-1}. The RMS increases to 2 mJy beam^{-1}close to the target and this local RMS noise has been used hereafter. This new low frequency radio map is shown in Figure 2a. We measure an integrated flux density of 15.19±1.52 Jy within $3\sigma_{RMS}$ contours and use a 10% flux density scale error. This value is in agreement with the integrated flux density of 15.0±1.5 Jy from TIFR GMRT Sky Survey (TGSS) at 154 MHz (Intema et al. 2017).

From Figure 2a, it can be seen that the central region shows an elongation in the north-south direction. This elongation shows up after the extraction process on the LoTSS-DR2 data set and is not real. The rest of the structure in the map matches very well with higher frequency maps and therefore does not seem to be affected by the extraction.

3.2. Archival data

3.2.1. Low resolution VLA 1.36 GHz and 4.85 GHz

We reprocessed archival VLA 1.36 GHz and 4.85 GHz data for the target. 1.36 GHz observations were carried out with the VLA in B configuration in November 1999 (Project code - GP022). The target was observed for ~11 hours with a 25 MHz bandwidth. 3C 48 and OQ 208 were the flux and phase calibrators respectively. 4.85 GHz observations of 3C 293 were carried out on November 1986 (Project code AB412) and October 1984 (AR115) in C and D configuration respectively. 3C 286 was used as the flux and phase calibrator for the AB412 data set. 3C 286 and OQ 208 were used as the flux and phase calibrator respectively for the AR0115 data sets. These were combined after cross-calibration was done individually on each data set to

include both long baseline for a high resolution and short baselines to recover large-scale emission from the source.

All data sets were reduced up till cross-calibration in Astronomical Image Processing System (AIPS, Greisen 2003). The data were manually flagged and the flux scale was set according to Perley & Butler (2013) as it is consistent with the Scaife & Heald (2012) scale at low frequencies. The self-calibration and imaging were performed in Common Astronomy Software Applications (CASA, McMullin et al. 2007) using the standard procedure[5] and the final images were obtained using Briggs weighting with a robust parameter of −0.5. The RMS noise is 0.08 mJy beam^{-1}and 0.22 mJy beam^{-1}for the 1.36 GHz and 4.85 GHz image respectively.

3.2.2. High resolution MERLIN

We have used the high resolution MERLIN image of the centre at 1.36 GHz made by Beswick et al. (2002) (data reduction procedure described therein), which has a resolution of 0.23''×0.20''. The integrated flux density of the central region estimated from the MERLIN image was 4.1 Jy, which is significantly higher than the integrated flux density of the central region from the low resolution VLA 1.36 GHz image (~3.75 Jy). To align the fluxes with previous measurements, we have used the VLA 1.36 GHz image at 1''resolution from Mahony et al. (2013). We estimated the integrated flux density in the two images using pyBDSF (Mohan et al. 2015) and then scaled the MERLIN image to the 1''image. We used a flux scale error of 5%. The final integrated flux density of the MERLIN image was 3.72±0.19 Jy with a local RMS noise of 1.2 mJy beam^{-1}.

3.2.3. High resolution VLA 4.85 GHz and 8.45 GHz

We have reprocessed VLA 4.85 GHz archival data to make a high resolution image of the central region at 4.8 GHz. 3C 293 was observed with the VLA in December 2000 (AT0249) and August 2002 (AH0766) in A and B configuration respectively. 3C 286 and OQ 208 were used as flux and phase calibrators respectively for both data sets.

VLA 8.45 GHz data for 3C 293 from observations on September 1991 (A configuration, Project code - AO0105) and December 1995 (B configuration, Project code - AK0403) was also reprocessed. 3C 286 was used as the flux calibrators for both data sets while 1144+402 and 1607+268 were used as the phase

---

[4] https://github.com/mhardcastle/ddf-pipeline

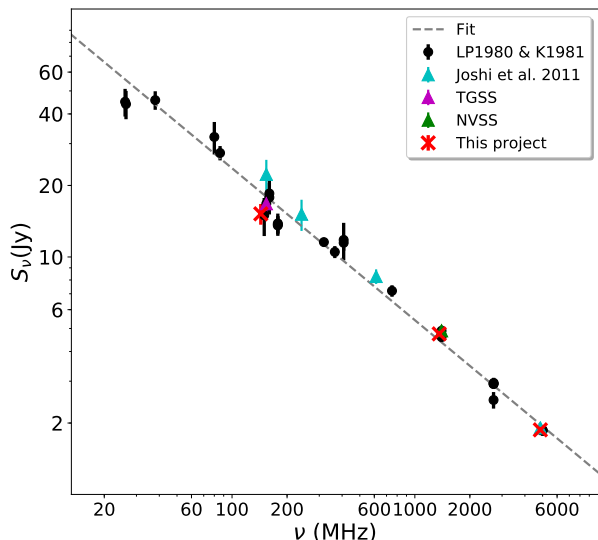[5] https://casaguides.nrao.edu/index.php/VLA_Self-calibration_Tutorial-CASA5.7.0

Figure 3: Integrated flux spectrum for 3C 293 from our images and literature. The red crosses are the integrated flux densities measured within the $3\,\sigma$ contours in our images, where σ is the local RMS noise. For the LOFAR HBA point at 144 MHz, only Dutch array data was used. Black circles are values from Laing & Peacock 1980 (LP1980) and Kuehr et al. 1981 (K1981). Cyan, purple and green triangles are values from the Joshi et al. (2011), TGSS (Intema et al. 2017) and NVSS (Condon et al. 1998) respectively. Flux densities from TGSS and this project were set to the Baars et al. (1977) flux scale for consistency. The dashed line shows the straight line fit using the values from literature (including TGSS and NVSS) and has a slope of -0.64 ± 0.01.

calibrators for the September 1991 and December 1995 observation respectively.

The flagging and cross-calibration for all archival VLA data sets were performed in AIPS and the flux scale was set according to Perley & Butler (2013). The cross-calibrated data sets were then combined to obtain a good uv-coverage and taken to CASA for self-calibration and imaging using Briggs weighting with a robust parameter of -0.5. The image statistics are summarised in Table 2. The flux scale errors used are 5% for the VLA 4.85 GHz and 8.45 GHz data.

3.3. Flux density scale

The accuracy of the flux scale is a key requirement for spectral index studies. To first confirm the flux scales of all our low resolution images, we have plotted the integrated flux densities of the entire source (centre + outer lobes) from our images along with values from literature (Laing & Peacock 1980; Kuehr et al. 1981) in Figure 3. Flux densities from the TGSS at 154 MHz (Intema et al. 2017) and NVSS at 1400 MHz (Condon et al. 1998) were also plotted alongside. The flux densities for our maps and a best fit line to the literature values are also shown. Although our integrated flux density at 144 MHz is in good agreement with the TGSS, as mentioned before, and other values from literature, it is significantly different from Joshi et al. (2011), who estimate the integrated flux density to be 22.3±3.4 Jy at 154 MHz. The difference between the flux density estimated from the best fit (dashed line in Figure 3) and the measured flux density (ΔS) is lower for our 144 MHz value ($\Delta S \approx 3.2$ Jy) than the 154 MHz Joshi et al.

(2011) value ($\Delta S \approx 4.4$ Jy). Due to the agreement of our flux densities with most of the literature, we consider our flux scale correct despite the discrepancy with Joshi et al. (2011).

As a sanity check, we have compared the integrated flux densities of the target from the high resolution images (see Table 2) with the integrated flux density of region C (see Table 3) from the low resolution images. We find that the flux scale is in agreement between the two images, which is in turn in agreement with literature.

Throughout the paper, errors in flux densities have been calculated using a quadrature combination of the noise errors and the flux scale errors. The noise error depends on the size of the integration area A_{int} (integration area in units of beam solid angle) and the RMS noise σ_{RMS} in the map as $\Delta S_n = \sigma_{\text{RMS}} \times \sqrt{A_{\text{int}}}$ (Klein et al. 2003). We use a flux scale error of 10% for LOFAR HBA, and 5% for VLA 1.36 GHz, 4.85 GHz and 8.45 GHz data (Scaife & Heald 2012; Perley & Butler 2013).

3.4. Spectral index maps

To spatially resolve the spectral properties, we have constructed spectral index maps using the low resolution images. Spectral index maps require images at the same resolution and range of uv-spacings, therefore all the images were smoothed to have a common resolution. Since an interferometer with minimum baseline D_{min} is sensitive to a largest angular scale of $0.6\,\lambda/D_{min}$ (Tamhane et al. 2015), we ensured that all the data we used was sensitive to angular scales $\gtrsim 250''$, which is the angular size of 3C 293.

We first smoothed the VLA 1.36 GHz and 4.85 GHz images to a resolution of $10.5''\times7''$ (BPA=90°), which is the LOFAR resolution and corresponds to a physical scale of ~9×6 kpc at the source redshift.

Phase calibration can cause position offsets between images of different frequencies. Such offsets can lead to systematic artefacts in the spectral index maps and therefore it is necessary to align the images and correct for such offsets. Ideally, point sources near the target are suited for this purpose, but since we do not have them in our field at all frequencies, we used the position of the peak flux density of the central region as reference. We fitted a 2D Gaussian on the central region to derive the pixel position coordinates of the peak flux density. We then used the coordinates of one image as reference and aligned all the others to it using the tasks IMHEAD and IMREGRID in CASA. After this, the positions matched with an accuracy of ≤0.01 pixels, which is sufficient for our analysis. Spectral index maps were then made using the task IMMATH in CASA using only the emission within the $5\,\sigma$ contours. The 144-1360 MHz and 1360-4850 MHz maps are shown in Figure 4. The 144-1360 MHz map shows steep index regions in the north and south edges of the centre, which are due to the artefact in the 144 MHz map, as discussed in Sect. 2.1.2.

The same procedure was followed to make spectral index maps using the high resolution images of the central region. We used the pixel position of the peak flux density of the eastern inner lobe for aligning the images. The 144-1360 MHz spectral index map is shown in Figure 5. At higher frequencies, the quality of our higher frequency spectral index maps for the centre was not good enough to allow us to perform a pixel by pixel analysis. Therefore, to probe the spectral properties, we have extracted integrated flux densities in regions across the centre, as shown in Figure 6. These flux densities were then used to calculate the spectral index in the regions. Regions E1, W1 and E2, W2 are on the inner lobes and diffuse emission respectively and O1 and O2 are on the outer north-western lobe. Comparing these
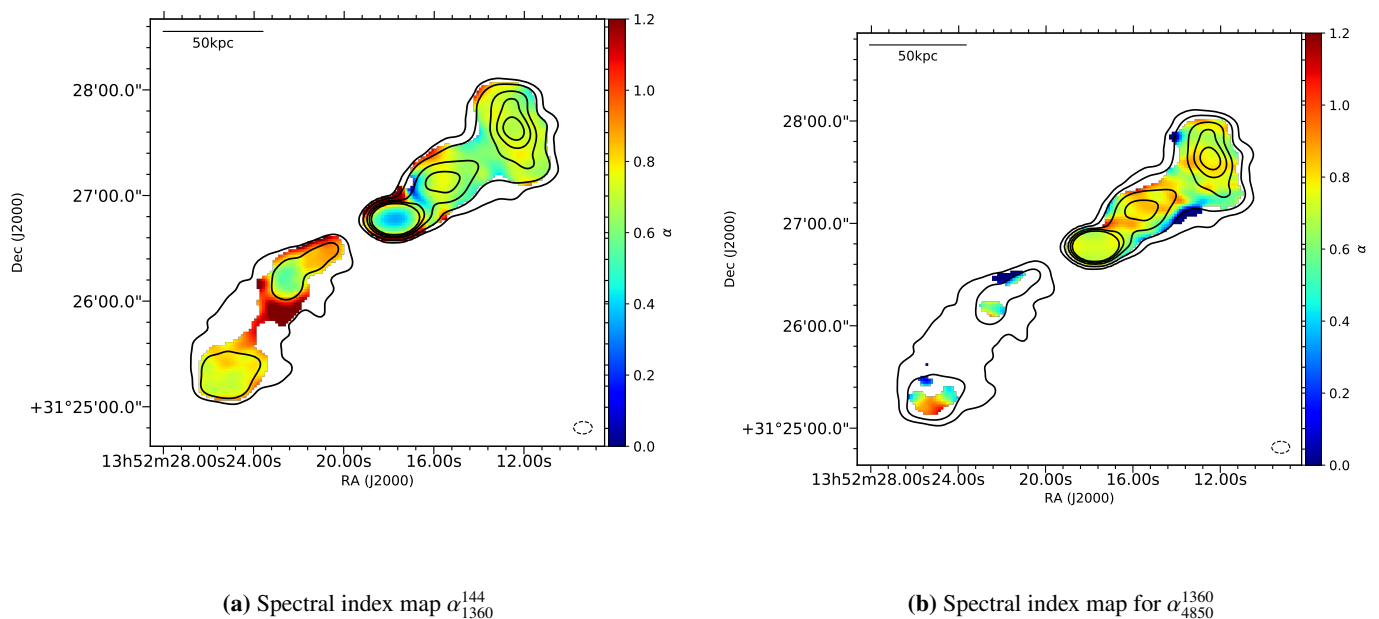
(a) Spectral index map α_{1360}^{144}

(b) Spectral index map for α_{4850}^{1360}

Figure 4: (a) The spectral index map from 144-1360 MHz and (b) 1360-4850 MHz for the large-scale lobes emission of 3C 293. All the maps are overlaid with contours of the 1360 MHz image at 10.5″×7″ resolution with the contour levels at (5, 30, 150, 350, 700)×σ_{RMS} where σ_{RMS}=0.09 mJy beam^{-1} is the local RMS noise. A flatter spectrum with $\alpha_{1360}^{144} < 0.5$ can be seen in the centre of the 144-1360 MHz map. The 1360-4850 MHz spectral index map does not include most of the southern lobe, since very little emission from the southern lobe is recovered at 4850 MHz.

regions to the high resolution image in Beswick et al. (2004), the core would lie in the W1 region. These regions and their sizes can be seen in Figure 6 and the extracted flux densities and spectral indices in Table 3. An integrated spectrum from 144 MHz to 4850 MHz comparing the central and outer lobe regions is shown in Figure 7.

Throughout the paper, errors in the spectral indices are calculated as :

$$\Delta\alpha = \frac{1}{\ln(\frac{\nu_1}{\nu_2})} \sqrt{\left(\frac{\Delta S_1}{S_1}\right)^2 + \left(\frac{\Delta S_2}{S_2}\right)^2}, \qquad (1)$$

where ΔS_1 and ΔS_2 are errors in the flux densities which include statistical errors in the measurements as well as uncertainties in the overall scale.

4. Results

In this section, we first describe the morphology of the large and small-scale emission in 3C 293. Then we estimate the magnetic field values for the source which are needed for the spectral ageing analysis. Then we describe the spectral index properties and the modelling of the spectrum.

4.1. Morphology

The large-scale morphology of the outer lobes and the small-scale morphology of the centre are discussed in the following sections.

4.1.1. Outer lobes

The large structure of 3C 293 is shown in Figure 2 at 144 MHz. The large-scale morphology is in agreement with what has been

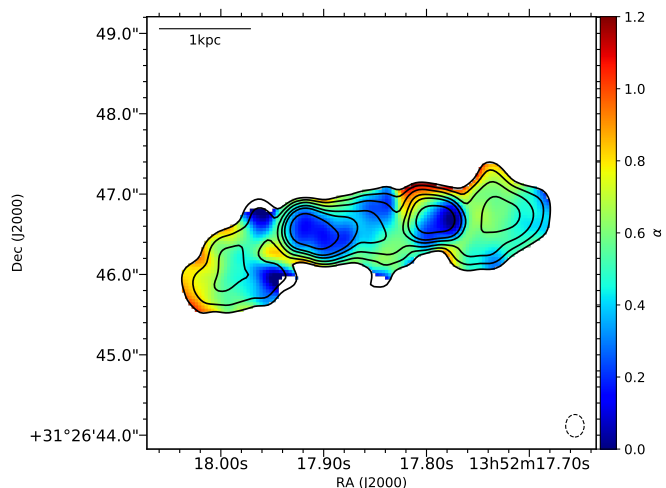**Figure 5:** Spectral index map of the high resolution central region of 3C 293 from 144-1360 MHz at 0.28″×0.23″ resolution. The map is overlaid with 1360 MHz contours with levels at: (5, 10, 20, 40, 65, 150)×σ_{RMS} where σ_{RMS} = 1.4 mJy beam^{-1} is the local RMS noise in the smoothed MERLIN image. The inner lobes clearly show a distinct spectral index population from the diffuse emission around them.

seen before at higher frequencies (Bridle et al. 1981; Joshi et al. 2011). The outer lobe emission in Figure 2a is ~250″ in to-
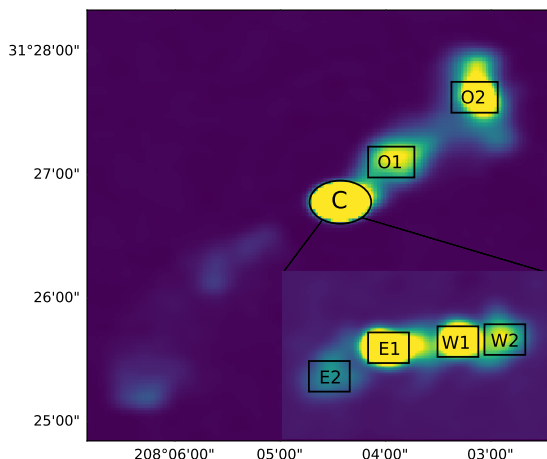
Figure 6: Regions used for extracting the fluxes in the low and high resolution images. Regions O1 and O2 of size 20″×15″and C of size 40″×25″were used to extract the fluxes after smoothing all images to the low resolution of 10.5″×7.0″. Regions E1, E2, W1 and W2 of size 0.8″×0.6″were used to extract the fluxes from the high resolution images at a resolution of 0.37″×0.36″. The continuum maps are at 1360 MHz.

Figure 7: Integrated spectra for the regions in the centre along the western lobe and outer lobe. Black lines show the spectra for central regions and red lines for outer lobe regions.

tal extent which corresponds to a physical size of ∼220 kpc at the source redshift (measured using 3σ contours as a boundary). The morphology is made up of a bright central region and two outer lobes, one in the north-west (∼84 kpc) and another in the south-east (∼107 kpc) direction. Despite increased sensitivity we do not obviously detect any new features in the low resolution LOFAR map. The bright emission at the end of the north-western lobe, covered by O2, extends in a direction perpendicular to the axis of the lobe. This bright region was suggested to be a hotspot before (for example Joshi et al. 2011; Lanz et al. 2015), although as discussed in Sec 3.2, the spectral properties do not confirm this. Using our 4.5″×4.1″resolution 1.4 GHz image, we also measure a physical size of ∼20 kpc for this region, which is larger than the typical sizes of ≲10 kpc for hotspots (for example Jeyakumar & Saikia 2000). These properties suggest that the large-scale radio emission in 3C 293 is not that of a typical FRII radio galaxy.

The south-eastern lobe also shows two regions of bright emission, although its total emission is fainter than its counterpart in the north. This asymmetry in intensity of the two lobes makes it very hard to image the south-eastern lobe and we do not have enough sensitivity at VLA 4.85 GHz to fully recover this emission. By looking at the contours, we can see a difference in the morphology of the emission bridge that connects the two bright emission regions at the ends of the lobe at 144 MHz (Figure 2a) and 1360 MHz (see contours in Figure 4a). The low significance of this feature and the uncertainty over its origin mean that at this moment, we are hesitant to conclude whether this difference in morphology is real or introduced during the self-calibration and imaging.

4.1.2. Central region

In Figure 2b, we show the high resolution map with LOFAR international stations at 144 MHz. This is the first time a resolved map of the central region has been made at such low frequencies. The total extent of the source is ∼4.5 kpc in physical size made
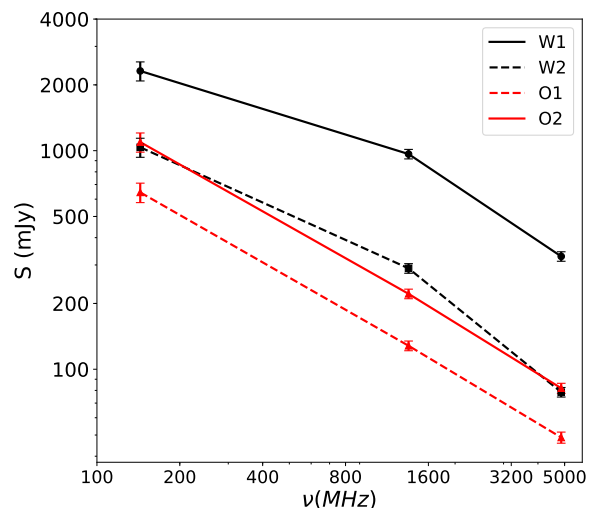
up of the two compact bright emission regions (referred to as the inner lobes henceforth), with lower brightness diffuse emission on either side. We do not detect any obvious new features in our low frequency map compared to high frequencies. The inner lobes have a physical size of ∼2 kpc in projection, with the core of the AGN located in the western inner lobe in region W1 of Figure 6 (Beswick et al. 2004).

4.2. Spectral properties

4.2.1. Outer lobes

To perform a resolved study of the spectral index in the outer lobes, we have constructed the spectral index maps shown in Figure 4 in the range 144-4850 MHz. The α_{1360}^{144} map (Figure 4a) shows a typical spectral index of 0.6-0.7 (±0.07) in the north-western lobe. In the α_{4850}^{1360} map (Figure 4b) this steepens to 0.7-0.8 (±0.06). As mentioned in Sect 2.5, we have also used regions O1 and O2 (see Figure 6) to calculate spectral indices. We find that the spectrum of the north-western lobe steepens from $\alpha_{1360}^{144}=0.72\pm0.05$ to $\alpha_{4850}^{1360} = 0.76\pm0.06$ for O1 and from $\alpha_{1360}^{144}=0.71\pm0.05$ to $\alpha_{4850}^{1360} = 0.78\pm0.06$ for O2. The integrated spectrum of these regions can be seen in Figure 7.

The first property to note here is the small curvature of the spectral index throughout the ∼90 kpc north-western lobe from 144-1360 MHz to 1360-4850 MHz, of $\Delta\alpha \leq 0.2$. There is also no sign of an ultra-steep spectrum (α_{1360}^{144} or $\alpha_{4850}^{1360} > 1.2$) anywhere in the north-western lobe. The second property is the lack of a spectral gradient throughout this lobe, with increasing distance from the centre, as can be seen in Figure 4. The spectral index appears to have a homogeneous distribution, at our resolution, which corresponds to a physical scale of ∼10 kpc. Another interesting property to note is the spectral index at the bright region at the end of the lobe (O2), which has been identified as a hotspot by previous studies. The spectral index of this emission does not show any flattening as would be expected from a hotspot. Despite the difference in flux density noted in Section 2.3, our spectral index results are consistent with Joshi et al. (2011).

Table 3: Flux densities and spectral indices for regions.

Region	$S_{144\,\mathrm{MHz}}$ (Jy)	$S_{1360\,\mathrm{MHz}}$ (Jy)	$S_{4850\,\mathrm{MHz}}$ (Jy)	$S_{8450\,\mathrm{MHz}}$ (Jy)	α_{1360}^{144}	α_{4850}^{1360}	α_{8450}^{4850}
E1	2.37±0.24	1.27±0.06	0.65±0.03	0.46±0.02	0.28	0.52	0.63
W1	2.32±0.23	0.97±0.05	0.33±0.02	0.21±0.01	0.39	0.84	0.80
E2	0.63±0.06	0.16±0.01	0.05±0.002	0.03±0.002	0.61	0.95	0.72
W2	1.04±0.10	0.29±0.01	0.08±0.004	0.05±0.002	0.57	1.02	0.95
O1	0.64±0.07	0.13±0.01	0.05±0.003	-	0.72	0.76	-
O2	1.09±0.11	0.22±0.01	0.08±0.004	-	0.71	0.78	-
C	10.70±1.07	3.84±0.19	1.53±0.08	-	0.46	0.72	-

Region column lists the regions as shown in Figure 6. The high resolution image (0.37″×0.36″) was used for the E1, E2, W1 and W2 and the low resolution image was used for O1, O2 and C. $S_{144\,\mathrm{MHz}}$, $S_{1360\,\mathrm{MHz}}$, $S_{4850\,\mathrm{MHz}}$ and $S_{8450\,\mathrm{MHz}}$ columns list the integrated flux densities, extracted from the regions at different frequencies. α_{1360}^{144}, α_{4850}^{1360} and α_{8450}^{4850} columns list the spectral indices. The $1\,\sigma$ errors in the spectral indices are ±0.05, ±0.06 and ±0.13 for α_{1360}^{144}, α_{4850}^{1360} and α_{8450}^{4850} respectively.

In the south-eastern lobe, α_{1360}^{144} is different from the north-western lobe. The outer edge has a spectral index of 0.7±0.05 which steepens to 0.8-0.9 (±0.05) moving towards the core. We see a region of very steep (dark red) spectral index ($\alpha_{1360}^{144} > 1$) just before the intermediate knot. This knot has a flatter spectral index of 0.6±0.05 followed by a region of 0.9±0.05 index moving towards the core. This spectral index distribution with multiple regions of flat and steep index is similar to that seen in FRIIs with episodic activity. The dark red spectral index region in this lobe is a result of the difference in spatial distribution of the flux density at 144 MHz and 1360 MHz and we do not have confidence in this feature, as described in Sect. 3.1.1. Furthermore, since we do not recover most of the emission in this lobe at 4850 MHz, we do not have confidence in the spectral index in Figure 4b and cannot perform spectral age modelling for it but discuss the spectral index from 144-1360 MHz for some regions in this lobe in Section 4.2.

4.2.2. Central region

The central region in the spectral index maps in Figure 4 shows an index of α_{1360}^{144}=0.4-0.5 (±0.05). This steepens to α_{4850}^{1360}=0.7-0.8 (±0.06). To investigate the spectrum in this region in more detail, we have used the higher resolution images. In the 144-1360 MHz spectral index map (Figure 5) we can clearly see two distinct spectral index populations (see Table 3 for regions) - the inner lobes with an index of $\alpha_{1360}^{144} \lesssim 0.3\pm0.05$, and the diffuse emission on either side with an index of α_{1360}^{144}=0.6-0.8 (±0.05). The resulting spectrum is shown in Figure 7.

As can be seen in Table 3, α_{1360}^{144} is 0.28±0.05 and 0.39±0.05 for the inner lobes regions E1 and W1 respectively, and α_{4850}^{1360} steepens to 0.52±0.06 and 0.84±0.06 respectively. These spectral index values are consistent with the spectral index value obtained by integrating over the entire central region C. The low frequency index of regions E1 and W1 is likely affected by absorption as it is well below the theoretical limit for injection index, which typically is 0.5. For the diffuse emission regions E2 and W2, α_{1360}^{144} is 0.61±0.05 and 0.57±0.05, respectively, while α_{4850}^{1360} is 0.95±0.06 and 1.02±0.06, respectively. Therefore, the central regions show a sharp break in their spectrum around

1360 MHz, and overall, the spectrum is steeper for the western regions in comparison to the eastern regions. The diffuse emission regions also show a steeper spectra than the inner lobe regions. A similar distinction in the spectra was also seen between 1.7-8.4 GHz by Akujor et al. (1996). This difference in the spectral index suggests a difference in the nature of these components and we discuss the absorption in section 3.4.2.

4.3. Magnetic field

The magnetic field is a crucial input to spectral ageing models, as the strength of the magnetic field affects how much the spectrum steepens over a period of time. Indeed, estimating magnetic fields for radio galaxies is difficult and usually, a simplifying assumption of equipartition between relativistic particles and the magnetic field is used (for example Jamrozy et al. 2007; Konar et al. 2012; Nandi et al. 2010, 2019; Sebastian et al. 2018). A detailed derivation for the equipartition magnetic field is given in Worrall & Birkinshaw (2006). X-ray emission from the outer lobes is used for a more direct probe for the magnetic field strength, since it is understood to originate from the inverse-Compton scattering between the relativistic electrons and the CMB photons (for example Feigelson et al. 1995; Isobe et al. 2002; Hardcastle et al. 2002; Mingo et al. 2017). In the last two decades, studies using IC-CMB X-ray emission have found that for FRII galaxies, magnetic field strengths are lower than the equipartition values by a factor of 2-3 (Croston et al. 2005; Ineson et al. 2017; Turner et al. 2017). However, the X-ray studies of some radio galaxies have also found magnetic field strengths close to the equipartition value (for example (Croston et al. 2005; Konar et al. 2009)). Since 3C 293 is not a typical FRII galaxy and X-ray studies of 3C 293 have only detected emission from small regions of the outer lobes (Lanz et al. 2015), which is not enough for this purpose, we have used the equipartition assumption. We acknowledge that the actual magnetic field in the outer lobes of 3C 293 might be sub-equipartition and discuss its effect on the derived spectral ages in Section 4.2. We have used the pySYNCH code[6], which is a python version of the SYNCH code

---

[6] https://github.com/mhardcastle/pysynch

(Hardcastle et al. 1998), to estimate the magnetic field strength in our synchrotron source (also see Mahatma et al. 2020).

For the outer north-western lobe, the integrated flux densities were used to fit a synchrotron spectrum. The lobe was assumed to be of cylindrical geometry with a length of 90″ and radius of 20″ (size measured using 5σ contours for reference). For the particle energy distribution, a power law of the form $N(\gamma) \propto \gamma^{-p}$ was used where γ is the Lorentz factor in the range $\gamma_{min} = 10$ to $\gamma_{max} = 10^6$ and p is the particle index and is related to the injection index in the synchrotron spectrum as $p = 2\alpha_{inj}+1$. We used Broadband Radio Astronomy Tools (BRATS[7]; Harwood et al. 2013, 2015) package to find the best fit injection index over the north-western lobe, which gave a best fit injection index of $\alpha_{inj} = 0.61\pm0.01$ (see Figure 8 and Sect. 3.4). This gives an equipartition magnetic field of $B_{NW} = 5.9^{+0.14}_{-0.13}\,\mu G$. This value is similar to the magnetic field strength of $5\,\mu G$ estimated by Machalski et al. (2016). Joshi et al. 2011 estimate a magnetic field of $11.2\,\mu G$, which is ~ 2 times higher than our estimate. This discrepancy is due to the difference in flux density discussed in Section 2.3. The magnetic field estimated for our data here is used as an input for the spectral ageing models discussed in Sect. 3.4.

We also estimated the equipartition magnetic field for the central regions shown in Figure 6 using a cylindrical geometry with a length of 0.8″ and a radius of 0.3″. An aged synchrotron spectrum was used to estimate the equipartition field instead of a powerlaw because it provided a better match to the curved spectra seen in these regions. For the inner lobe regions, the 144 MHz data point was not used because it is affected by absorption, which makes it very hard to estimate the injection index. We used an injection index of $\alpha_{inj} = 0.5$, which is the theoretical limit for injection indices found for plasma in radio galaxies because absorption in the inner lobes (see Sect. 3.5.1 and 4.1.1) erases any information about injection. For regions E1 and W1, $B_{E1} = 237^{+13}_{-9}\,\mu G$ and $B_{W1} = 218^{+17}_{-14}\,\mu G$ were obtained respectively. For the diffuse emission regions, the low frequency index was used as the injection index, however it is possible that this value is affected by absorption and the actual injection index is steeper. For E2 and W2, $B_{E2} = 158^{+15}_{-13}\,\mu G$ and $B_{W2} = 176^{+16}_{-14}\,\mu G$ were obtained respectively. To check the robustness of our estimates, we repeated the calculations using regions of various sizes and obtained field strengths that are in agreement with each other.

4.4. Modelling of spectra

4.4.1. Spectral age modelling

The shape of the energy spectrum of the electron population can help investigate the evolution of the plasma in radio galaxies. In a system of particles emitting synchrotron radiation under a magnetic field, the energy loss is higher for high energy particles ($dE/dt \propto \nu^2$) which steepens the spectrum at the higher frequency end. Presence of steep spectra has been used as an indicator for old remnant plasma, devoid of any fresh particle injection. The presence of old plasma along with a region of newer plasma has also been used as evidence for multiple phases of AGN activity.

Spectral modelling can be used as a probe for estimating particle ages for an electron population undergoing synchrotron and inverse-Compton losses assuming no new injection. We have used the JP model (Jaffe & Perola 1973) here, which assumes that the pitch angle of the magnetic field has a time dependence,
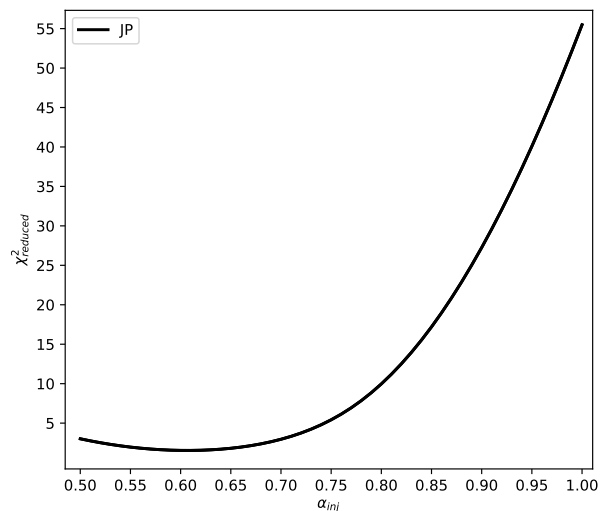
Figure 8: Reduced χ^2 values for the varying injection index values for the north-western lobe of 3C 293, averaged over the regions. The data points are taken at an interval of 0.01 between 0.5 and 1.0, and the minimum occurs at 0.61 for both JP and Tribble models. The reduced χ^2 values for the two models are very similar, therefore only the JP model values are shown here.

which is a realistic assumption for plasma with a lifetime of millions of years. Another model we have used is by Tribble 1993, that allows the electrons to age under a varying magnetic field structure with a Gaussian random distribution (see Harwood et al. 2013; Hardcastle & Krause 2013). A common assumption in these models is that of a single injection event in the past, which can only be physically realistic over small scales of a few kpc.

To investigate the spectral ageing of the outer north-western lobe, caused by the natural ageing of plasma due to radiative losses, we have used the BRATS package (Harwood et al. 2013, 2015). We fitted the JP and Tribble models over the entire north-western lobe in a pixel-by-pixel manner to perform a spatially resolved analysis. The assumption of a single injection event and particles being accelerated in the same event can work reasonably well on the scales of our pixel-by-pixel analysis, that is 1.5″ pixel corresponding to 1.3 kpc. We first derived the best fit injection index, α_{inj} to be used in the models. For this, we performed a series of fits over the north-western lobe using JP and Tribble models in BRATS, keeping all the other parameters constant and varying α_{inj} from 0.5 to 1 with a step size of 0.1. After we found a best fit injection index in this range, we reduced the step size to 0.01 to search around the previous value. The injection index vs reduced χ^2 for the two models is shown in Figure 8. The plot shows a minimum at $\alpha_{inj} = 0.61\pm0.01$ for the two models, with an average reduced χ^2 of 1.53 for both JP and Tribble models. We use this value as the injection index for our spectral age models.

Using the best fit injection index and the equipartition magnetic field from Sect. 3.3, we fitted the JP and Tribble models over the entire north-western lobe. Spectral age modelling typically requires data at 5 frequencies - 2 below the break to fix the injection index and 3 above the break to measure the curvature due to radiative losses. Although we use only 3 frequencies, our model fit provides reasonable results but likely denote up-
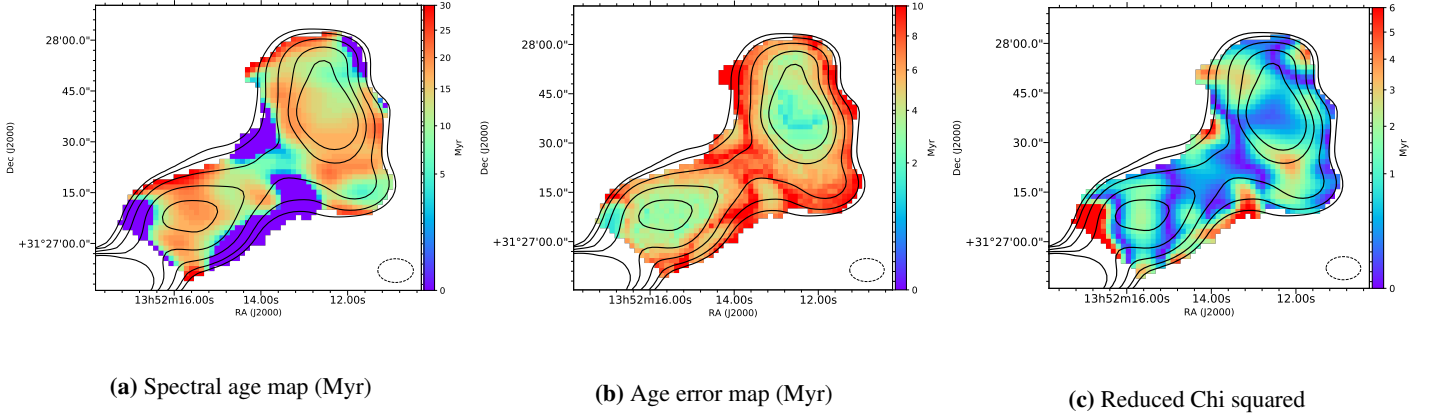
(a) Spectral age map (Myr)   **(b)** Age error map (Myr)   **(c)** Reduced Chi squared

Figure 9: (a) Spectral age map of the north-western outer lobe of 3C 293, (b) age error map and (c) reduced χ^2 map (right) using the JP model. Overlaid are 1360 MHz emission contours at $10.5'' \times 7''$ and at levels $(30, 50, 100, 200, 350) \times \sigma_{\text{RMS}}$.

Table 4: Spectral ageing model fit results for the north-western lobe

Model	Average χ^2_{reduced}	Confidence bins					Rejected	Median confidence
		<68	68-90	90-95	95-99	≥ 99		
JP	2.26	699	399	107	57	44	No	<68
Tribble	1.77	783	372	68	47	36	No	<68

'Model' column lists the spectral ageing model fitted to the data. 'Average χ^2_{reduced}' column list the average χ^2_{reduced} of the fit over the entire lobe. 'Confidence bins' columns list the number of regions for which the χ^2 falls within the labelled confidence range. 'Rejected' column lists whether the goodness of fit can be rejected over the entire source. 'Median confidence' column lists the median confidence level at which the model cannot be rejected.

Table 5: Absorption model fit results for inner lobe regions

Model	Region	a	α	β	ν_{p} (GHz)	χ^2_{reduced}
Homogeneous FFA	E1	1.52±0.05	0.55±0.02	...	0.116±0.009	0.36
	W1	1.25±0.02	0.84±0.01	...	0.145±0.004	0.11
Internal FFA	E1	1.53±0.05	0.55±0.02	...	0.171±0.015	0.35
	W1	1.25±0.03	0.84±0.01	...	0.225±0.008	0.11
SSA	E1	4.14±0.22	...	-2.10±0.05	0.161±0.010	0.38
	W1	4.96±0.12	...	-2.67±0.02	0.189±0.003	0.09

'Model' lists the absorption model fit to the data. 'Region' lists the inner lobe regions, E1 (eastern) or W1 (western). 'a', 'α', 'β' and 'ν_{p}' list the best fit model parameters obtained along with 1σ errors. 'χ^2_{reduced}' is the reduced chi-square obtained for the fit.

per limits to the spectral ages. The fitting results are presented in Table 4 and the spectral age maps obtained with the JP model are shown in Figure 9. The fits obtained using the Tribble model gave results similar to the JP model and therefore we have not shown those maps here. From the table it is clear that none of the models can be rejected at the 68% confidence level over the entire lobe. The red pixels in the reduced χ^2 map (Figure 9c) correspond to the regions that can be rejected at ≥ 95% level. These regions amount to 7% of the total regions in the lobe. From the spectral age map, we conclude that the spectral ages for most of the north-western lobe lie between 10-20 Myr, especially for the two bright regions in the lobe. The median age for the regions

for which the models cannot be rejected with >90% confidence is 13.1 Myr. We find that spectral ages do not show a gradient with distance from the centre. Some regions show no or very little spectral ageing, however, the associated high errors and reduced χ^2 values reduce our confidence in the model fits over these regions.

For the central regions, we use the following equation (Kardashev 1962; Murgia et al. 2011) -

$$t_{\text{s}} = 1590 \frac{B_{\text{eq}}^{0.5}}{(B_{\text{eq}}^2 + B_{\text{CMB}}^2)\sqrt{\nu_{\text{b}}(1+z)}}, \quad (2)$$

where t_s is in Myr, the magnetic fields B_{eq} and $B_{CMB}=3.25\times(1+z)^2$ are in μG, and the break frequency ν_b is in GHz. Assuming the break frequency to be the highest frequency of our observations, that is 8.45 GHz, we estimate upper limits on the spectral ages - $\lesssim 0.15\pm0.01$ Myr for E1, $\lesssim 0.17\pm0.02$ Myr for W1, $\lesssim 0.27\pm0.04$ Myr for E2 and $\lesssim 0.23\pm0.03$ Myr for W2. Machalski et al. (2016) estimate a dynamical age of ~ 0.3 Myr for the central region. Their estimate is similar to ours within errors, but they do not include the absorption in the spectra, which makes it difficult to compare the two ages. The difference from their value could also be due to the different in the magnetic field strength estimated between the two studies.

4.4.2. Absorption models for inner lobes

The spectra for the inner lobe regions E1 and W1, are relatively flat in the 144-1360 MHz range and below the theoretical limit for injection index ($\alpha_{inj} = 0.5$). This suggests that the spectra peaks in between 144 and 1360 MHz which implies the presence of low frequency absorption. An absorbed spectrum is seen compact steep spectrum (CSS) or gigahertz peaked spectrum (GPS) radio galaxies. This peak (or turnover) is attributed to the absorption of synchrotron radiation in the source, which is broadly a manifestation of either synchrotron self absorption (SSA) or free-free absorption (FFA) (Kellermann et al. 1966; Tingay & de Kool 2003; Callingham et al. 2015).

The best way to identify the absorption mechanism is to measure the slope of the spectrum below the peak frequency: since FFA shows a much steeper index ($\alpha \lesssim -2.5$) than SSA. Given the lack of more high resolution observations below 144 MHz, we cannot directly estimate the spectral index below the peak. Therefore, we have fitted various absorption models to the spectra for E1 and W1, similar to Callingham et al. (2015) and used the derived fit parameters to discriminate between these models in Section 4.1.1.

1. Synchrotron Self Absorption (SSA) - This is a standard SSA model that assumes self absorption from a synchrotron emitting plasma due to the scattering of the emitted synchrotron photons by the relativistic electrons. The absorption cross section is higher for longer wavelengths and therefore as the observing frequency increases, photons emerge from the deeper regions of the source until the optically thin regime is reached. This model for a synchrotron emitting homogeneous plasma is given by -

$$S_\nu = a\left(\frac{\nu}{\nu_p}\right)^{\frac{\beta+1}{2}}\left(\frac{1-e^{-\tau}}{\tau}\right), \qquad (3)$$

where

$$\tau = \left(\frac{\nu}{\nu_p}\right)^{\frac{\beta-4}{2}}. \qquad (4)$$

We note that ν_p is the frequency at which the source becomes optically thick ($\tau=1$), β is the power law index of the electron energy distribution related to the synchrotron spectral index as $\alpha = -(\beta + 1)/2$ and τ is the optical depth.

2. Homogeneous Free Free Absorption (FFA) - This model assumes that the attenuation of radiation is caused by an external homogeneous ionised screen around the relativistic plasma emitting the synchrotron spectrum. The free-free absorbed spectrum is then given as -

$$S_\nu = a\nu^{-\alpha}e^{-\tau_\nu}, \qquad (5)$$

where a and α are the amplitude and spectral index of the intrinsic synchrotron spectrum, and τ_ν is the optical depth. The optical depth is parameterised as $\tau_\nu = (\nu/\nu_p)^{-2.1}$, where ν_p is the frequency at which the optical depth is unity.

3. Internal FFA - In this case, the absorbing ionised medium is mixed with relativistic electrons that produce the synchrotron spectrum. This model is given as -

$$S_\nu = a\nu^{-\alpha}\left(\frac{1-e^{-\tau}}{\tau}\right). \qquad (6)$$

To fit these models to the inner lobes, we used the integrated flux densities and their errors, extracted from regions E1 and W1 and summarised in Table 3. The absorption models were then fitted to the data using the SciPy python package which utilises the Levenberg–Marquardt optimisation method. The resulting model fits are shown in Figure 10 and the fit parameters are summarised in Table 5. Both SSA and FFA models provide similar quality fits to our data. We find that for all three models, the ν_p frequency, the frequency at which optical depth is 1, is systematically higher for the western lobe than the eastern lobe, with a 3σ significance. To test the robustness of our analysis, we performed the same fitting procedure to integrated fluxes from regions of different sizes in the inner lobes and found that our results were in agreement. The results of the models and their implications for the inner lobes will be discussed further in Sect. 4.1.

5. Discussion

The evolution of the radio emission in 3C 293 is complex and our results confirm this. Here we discuss the results of our spectral analysis going from the inner to the outer scale emission in the context of understanding the life-cycle and evolutionary scenarios for 3C 293.

5.1. Interplay of radio plasma and gas in the central region

3C 293 shows bright radio inner lobes surrounded by diffuse emission, with a total linear extent of ~ 4.5 kpc. These compact components have flat low frequency spectra (Section 3.5) and are surrounded by a dense and rich ISM. Previous studies have found evidence for jet-ISM interaction in the galaxy. In their study of ionised gas kinematics, Mahony et al. (2016) found jet-driven outflows and disturbed gas throughout the central region of the host galaxy. Outflows of warm gas have also been observed in the galaxy by Emonts et al. (2005). In the neutral gas, Morganti et al. (2003) found fast outflows, up to 1400 km s^{-1}, in central regions and also suggest that it is driven by the interaction between the radio jets and the ISM. More recently, Schulz et al. (2021) have also used global VLBI to map the HI outflow in the galaxy. Lanz et al. (2015) studied the galaxy in X-ray and found more evidence for jet-ISM interaction. They concluded that the X-ray emission from the central region is caused by shock heating of the gas by this interaction. Massaro et al. (2010) also observed X-ray emission from the radio jets. Here, we explore what the spectral properties of these components tell us about the system.

5.1.1. What causes absorption in the inner lobes?

As discussed in Section 3.4.2, we have used our model fit parameters to discriminate between the SSA and FFA models.

(i) SSA : From the fit parameters obtained for SSA in Sect 3.4.2 (see Table 5) we derive a peak frequency of 220 MHz and
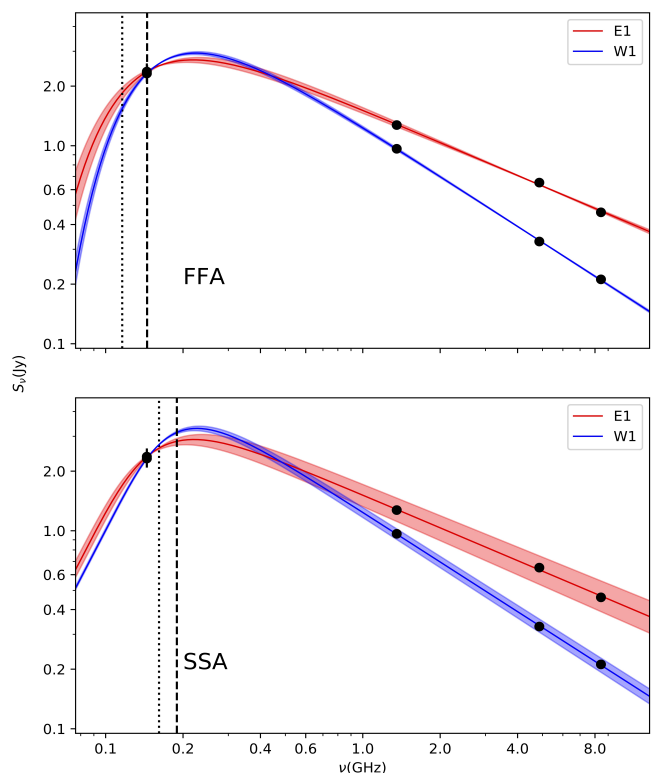
Figure 10: Best fits of Homogeneous FFA (top panel) and SSA (bottom panel) absorption models to the E1 (eastern) and W1 (western) inner lobes regions of 3C 293. A peak in the spectrum can be seen at 220-230 MHz. All models provide similar quality fits to the data. The vertical lines show the ν_p frequency, for E1 (dotted) and W1 (dashed). ν_p is the frequency at which optical depth $\tau = 1$, an is therefore a measure of the optical depth. From the model fits, ν_p for W1 is systematically higher than for E1.

226 MHz for E1 and W1, respectively. If SSA is the origin of the turnover, we can now relate these parameters to the properties of the source. For pure SSA, in a homogeneous synchrotron self-absorbed radio source, the magnetic field B is related to the peak frequency ν_{peak} and the flux density at the peak frequency S_{max}. Under an equipartition assumption between magnetic field and the electrons, the peak frequency is given by (Kellermann & Pauliny-Toth 1981; Callingham et al. 2015)

$$\nu_{\text{peak}} \sim 8.1 B^{1/5} S_{\text{max}}^{2/5} \theta^{-4/5} (1+z)^{1/5}, \qquad (7)$$

where ν_{peak} is in GHz, B is the magnetic field in G, S_{max} is the peak flux density at the peak frequency in Jy and θ is the angular size of the source in mas. The relation depends very strongly on observables such as angular size and peak frequency, which are very difficult to estimate accurately. Therefore, the computed magnetic field strengths should be treated with care.

We use $\theta = 692.8$ mas, which is estimated using $\theta = \sqrt{\theta_1 \theta_2}$, where $\theta_1 = 800$ mas and $\theta_2 = 600$ mas are the two dimensions of the regions. We estimate a magnetic field of 4.9×10^2 G for E1 and 4.3×10^2 G for W1 region. Using more accurate sizes of the inner lobes from the 30 mas high resolution images from Beswick et al. (2004), equal to ~400 mas, we estimate magnetic fields 2-8 times lower. However, these values are significantly higher than our equipartition estimates in Section 3.3, by ~10^7. Our estimates from SSA are also at least 10^3 times higher than the typical values found in GPS sources, which are in the

range 5-100 mG (O'Dea 1998; Orienti & Dallacasa 2008). For CSS sources of similar sizes and peak frequencies from O'Dea (1998), such as 3C 48, 3C 138 and 3C 147, we estimate magnetic field strengths of $\approx$ 4-15 mG using equation 6.

For a sample of young radio sources, Orienti & Dallacasa (2008) find good agreement between equipartition magnetic fields and those derived using the peak frequency assuming SSA thus concluding that the turnover in their spectra is probably due to SSA. However, for a couple of their sources (J0428+3259 and J1511+0518), the magnetic fields from SSA relation were significantly higher than the equipartition values and they suggest that for these sources, a more likely explanation is that the spectral peak is caused by free-free absorption.

The unrealistically high magnetic field strengths estimated assuming SSA cannot sustain synchrotron emission in the system (loss lifetimes of $< 3 \times 10^{-4}$ yr), even for the light travel time across the region. This tells us that it is unlikely that SSA is the dominant or only absorption mechanism in the inner lobes of 3C 293.

(ii) FFA : Free-free absorption requires the presence of a dense optical line-emission medium and strong depolarisation of the radio source. Multiple studies have found a dense medium in the central few kpc of 3C 293 (Emonts et al. 2005; Labiano et al. 2014; Mahony et al. 2016) and Akujor et al. (1996) have confirmed strong depolarisation in the source which may be caused by the gaseous disc revealed by optical emission lines.

From our best fit results in Table 5 (also see vertical lines in Figure 10), we find that the optical depth is systematically higher for W1 than E1 with a 3σ significance. Over the years, resolved absorption studies of CSS/GPS sources have found that a difference between the optical depths of the lobes is due to the larger path length in the ionised medium along the line of sight for the emission from the receding lobe, for example OQ 208 (Kameno et al. 2000), NGC 1052 (Kameno et al. 2001), 3C 84 (Vermeulen et al. 1994; Walker et al. 1994, 1999), NGC 4261 (Jones et al. 2000, 2001) and NGC 6251 (Sudou et al. 2001) (and also see Figure 6 of Kameno et al. 2000). The asymmetry in the derived optical depths is consistent with the current understanding of the orientation of the inner jets (Beswick et al. 2004; Mahony et al. 2016).

In their study of FFA in GPS sources, Kameno et al. (2005) found that the ratio of the optical depths of the lobes (τ_A / τ_B) is < 5 for sources where the line of sight is nearly perpendicular to the jet axis. We find an optical depth ratio of ~1.6 between the inner lobes, which shows that this is not a case of highly asymmetric FFA.

Beswick et al. (2004) in their high resolution study of the inner lobes also attribute the steeper index of the western jet to the presence of FFA. In the case of FFA from an external homogeneous ionised screen, the emission measure of the absorbing medium is given as (O'Dea 1998)-

$$n_e^2 L = 3.05 \times 10^6 \tau \left(\frac{T}{10^4 K}\right)^{1.35} \left(\frac{\nu}{1\, GHz}\right)^{2.1} \text{cm}^{-6}\text{pc}, \qquad (8)$$

where n_e is the electron density in cm^{-3}, L is the path length in pc, τ is the optical depth at frequency ν in GHz. FFA in galaxies is generally attributed to the Narrow Line Region (NLR) clouds around the radio jets and a filling factor f has been included in the path length to account for the clumpy nature of the absorbing medium. We estimate a value of $f = 4.3 \times 10^{-6}$ using a narrow line Hβ luminosity of L(Hβ)$_{\text{narrow}} = 1.3 \times 10^{40}$ ergs s^{-1} and $n_e = 200$ cm^{-3} from Emonts et al. (2005). Using these parameters, we estimate a path length of $\approx$50 pc for E1 and $\approx$80 pc for W1.

These path lengths are easily achievable given the evidence for narrow line region clouds out to a few kpc and a dense ISM (Emonts et al. 2005).

In their study of alternative FFA models, Bicknell et al. (1997) found that the optical depth in a free-free absorption screen will vary with radius if the medium around the radio source is affected by shocks. Previous studies have confirmed the presence of shocks in the medium surrounding inner lobes of 3C 293 (Lanz et al. 2015; Mahony et al. 2016). Thus it is possible that the difference we see in the optical depths for the two lobes is a consequence of inhomogeneous FFA. However, given the limitations of our current data sets, we cannot investigate this effect further and would need more high resolution observations below the peak frequency to discriminate between the two FFA models.

In case of FFA being responsible for the spectral turnover, ν_{peak} due to SSA would be lower with a higher peak flux density S_{max} than observed. The magnetic field from equation 5 depends on these observables as $B \propto \nu_{\text{peak}}^5 S_{\text{max}}^{-2}$, and therefore the true field strength would be less than estimated using the observed peak and attributing it to SSA. This would explain the unrealistically high magnetic fields estimated from equation 5. We conclude that the most realistic situation is that FFA is dominant but is likely not the sole absorption mechanism and SSA also contributes a component to the absorbed spectrum.

5.1.2. Are the inner lobes a young source?

Akujor et al. (1996) have speculated the presence of a CSS source in the inner lobes which are ~2 kpc in size and contribute a significant fraction to the total flux density. Even higher (mas) resolution images of the inner lobes at 1.4 GHz and 4.5 GHz have found bright jet emission and radio knots in this region (Akujor et al. 1996; Beswick et al. 2004) towards the end of the jet, which tells us that the inner lobes are jet dominated.

Multiple studies of CSS and GPS sources have found a correlation between the linear size of the source and the peak frequency of the spectrum, in both high power (Bicknell et al. 1997; O'Dea & Baum 1997) and low power (De Vries et al. 2009) sources. Although this correlation has been explained in terms of SSA (Snellen et al. 2000; Fanti 2009), FFA models with absorption due to an inhomogeneous medium have also been able to recreate the relation (Bicknell et al. 1997; Kuncic et al. 1997). However, FFA via a homogeneous external medium cannot replicate such a relationship (O'Dea 1998). This correlation is given by -

$$\log(\nu) = -0.21(\pm 0.05) - 0.65(\pm 0.05)\log(L_{PLS}), \quad (9)$$

where L_{PLS} is the linear size in kpc and ν is the peak frequency in GHz. We deproject our linear size by using the viewing angle with respect to the jet axis, estimated to be 55° and 75° by Beswick et al. (2004) and Machalski et al. (2016), respectively. This gives a deprojected physical size of 2.1-2.4 kpc. The minimum peak frequency corresponding to this is 349^{+26}_{-24} MHz. This is significantly higher than the rest frame peak frequencies of 230-240 MHz for the inner lobes that we estimate from the absorption models in Section 3.4.2. This suggests that the inner lobes are strongly interacting with and prevented from expanding by, the rich surrounding medium of the host galaxy, also found by other studies mentioned before.

As discussed in Sect. 3.4.1, we obtained ages of $\lesssim 0.15 \pm 0.01$ Myr for E1 and $\lesssim 0.17 \pm 0.02$ Myr for W1. However, for 3C 293, Emonts et al. (2005) have estimated that jet induced

outflows, for a constant velocity, must have been driven for ~1 Myr in order to obtain the total outflow mass of HI and ionised gas. Our spectral ages are much lower than their estimate, but it is possible that older phases of jet activity have contributed to the outflow mass or that the velocity of the gas has decreased with time and expansion of the outflow. The spectral ages are in agreement with jet dominated CSS sources of similar sizes found by Murgia et al. (2002), who found ages in the range of 10^3 to 10^4 yr, and attributed them to the bright jet components. This tells us that the spectral ages we estimate do not represent the actual source age, but the permanence time of the electrons in the bright compact jet components which dominate the flux density and where the electron reacceleration occurs. This again supports a scenario where jet-ISM interaction impedes the flow of plasma.

It is unlikely that these lobes are just strongly interacting and not young, that is they are as old as the large-scale radio galaxy. This scenario also supports FFA by the rich surrounding medium being the dominant absorption mechanism, as we discussed in Sect. 4.1.1. Other properties such as depolarisation at high frequencies, Faraday dispersion of $\Delta < 1200$ cm$^{-3}\mu$G pc and minimum pressures in the inner lobes of 3C 293 are also typical of CSSs (Akujor et al. 1996).

5.1.3. What is the origin of diffuse emission around inner lobes?

The morphology of the regions adjacent to the inner lobes (W2 and E2) is intriguing. There is an abrupt increase in the width of the emission and reduction in the surface brightness compared to the inner lobes. The α_{1360}^{144} spectral index of the diffuse emission also shows a steepening with respect to the inner lobes. Assuming that the emission from E2 and W2 is optically thin, the spectral age is $\lesssim 0.27 \pm 0.04$ Myr for E2 and $\lesssim 0.23 \pm 0.03$ Myr for W2, as discussed in Sect. 3.4.1. The steeper spectra and the morphology of the diffuse emission regions suggest that they could be from an older phase of activity. These diffuse regions representing an older phase of activity was also suggested by the spectral study of Akujor et al. (1996).

Another plausible scenario is that the diffuse regions are formed by the leaked plasma from the radio jet as it propagates through the galaxy's disk. In their study of simulated interaction between a jet and the galaxy's disk, Mukherjee et al. (2018) found that a jet inclined to the plane of the disc will interact strongly with the gas in the disc and will not immediately clear the medium and move out. It will deflect and decelerate, with plasma leaking out along the path of least resistance (see their Figure 14). It is likely that this is the case for 3C 293, where the jets are inclined with respect to the host galaxy's disc (Floyd et al. 2005; Labiano et al. 2014). Leakage from the decelerated plasma that moves out of the disk, in directions perpendicular to the jet flow, would form the lower surface brightness diffuse emission we see in these regions. Another prediction of the simulation from Mukherjee et al. (2018) is the presence of outflows, as seen in 3C 293 and described before.

5.2. Evolution of the outer lobes

From Figure 9, we observe spectral ages varying typically from ≈10-20 Myr over the two bright regions (also marked by O1 and O2) of the north-western outer lobe, with a median age of 13.1 Myr. Machalski et al. (2016) have estimated the dynamical age to be ~62 Myr, which gives a dynamical to spectral age ra-

tio between ~3 and ~6 for most of the lobe. It is possible that this difference is a result of the equipartition assumption for the magnetic field. Indeed, in their study of spectral and dynamical ages, Mahatma et al. (2020) found that the equipartition assumption can underestimate the spectral age by factors of up to ~20 and that the actual magnetic field strength in FRII galaxies is sub-equipartition.

In order to understand the evolution of the outer lobes, there are two important spectral properties to note (Section 3.2.1). The first property is the small curvature from 144 MHz to 4850 MHz. We do not see any sign of an ultra-steep spectral index (α_{1360}^{144} or $\alpha_{4850}^{1360} > 1.2$) up to 5 GHz. The second property is lack of a dependence of the spectral index on distance from the centre, which seems to be uniformly distributed on a scale of about 10 kpc throughout the 90 kpc lobe.

The absence of any ultra steep spectral index suggests that the outer lobes are not remnants. The lack of a spectral gradient is contrary to the trend expected, as plasma in different regions would have different ages and would be expected to show different curvatures in their spectra. This suggests that the plasma in the lobe is highly turbulent which reaccelerates old electrons (due to shock acceleration) and mixes different electron populations. The diffuse morphology of the north-western lobe also suggests that the flow is not very well collimated and more turbulent.

Such scenarios have been suggested to be active in galaxies with similar properties (bright resolved inner kpc region and outer, low-surface brightness, diffuse lobes), for example Centaurus A (McKinley et al. 2018), B2 0258+35 (Brienza et al. 2018) and more recently NGC 3998 (Sridhar et al. 2020). For Centaurus A, Eilek (2014) have estimated that in case of a lack of injection of fresh plasma, the turbulence would last a few tens of Myr (~30 Myr) after which the lobes will fade away. Keeping in mind that the size of 3C 293 (~220 kpc) is much smaller than that of Centaurus A (~500 kpc), it is likely that these processes could be active in the outer lobes of 3C 293. The presence of shocks in the outer lobes of 3C 293 has been suggested by Lanz et al. (2015), who in their study of X-ray emission from 3C 293, concluded that the presence of shell-like morphological features in the outer lobes and their possible thermal origin mean that they could be associated with bowshocks, that heat the gas to X-ray temperatures.

Keeping the spectral properties in mind, we propose two scenarios for the evolution of the outer lobes of 3C 293. One scenario here does not preclude the other.

1. The outer lobes represent older phases of activity. In this scenario, the interruption would have happened for a very short time, possibly only a few Myr ago (~0.7 Myr from Machalski et al. 2016), which would explain the lack of an ultra steep spectral index anywhere in the lobe. As mentioned in Section 3.1.1, the bright emission at the end of the lobe (O2) has peculiar morphology which could mean that it is from an older phase of activity, or represents a variable and intense phase of activity. The lack of a spectral gradient would be due to the shocks caused by the newer jet material expanding (O1) into the older lobe material (O2), supersonically. This would also explain why such spectral properties are not observed in other restarted radio galaxies which are hydrodynamically not as complex as a galaxy with several episodes of jet restarting and are powered by a single constant flow. In this scenario, the young CSS source in the inner lobes of 3C 293 would be formed in a newer phase of activity.

2. The AGN has not switched off completely, and the outer lobes are still fuelled by the centre. The jet flow is intermittent due to a strong interaction between the jets and the dense ISM. In this scenario, the fuelling of the lobes by the centre would explain the lack of a steep spectra or a strong curvature. The strong interaction of the jets with the dense ISM would disrupt the flow and trap the plasma, building up a deposition of energy until the plasma finally breaks through and expands in the outer lobes. The decollimation of the jet flow due to the interaction would result in a turbulent flow of plasma in the outer lobe. This would also explain the abrupt change in the surface brightness of the jets outside the nuclear region. However, in this scenario, the fuelling of the outer lobes by the centre would be needed to maintain the turbulence that keeps the spectra from steepening. We do not see any direct extension of the diffuse emission in the centre to the outer lobes, therefore we cannot confirm the presence of an open plasma transport channel to these lobes. It is possible that we do not have enough sensitivity in our sub-arcsecond images to recover such lower surface brightness emission and therefore, we cannot rule out the presence of such a plasma transport channel.

As mentioned before in Section 3.2.1, the spectral index distribution in the south-eastern lobe suggests multiple episodes of jet activity, similar to the north-western lobe. The presence of similar X-ray features in this lobe (Lanz et al. 2015) also suggests that similar processes are active here.

5.3. 3C 293 and other similar galaxies

3C 293 appears to belong to the growing group of radio galaxies, that were classified as restarted based on their morphology (bright central region and low surface brightness diffuse lobes) and have been found to show no curvature in the radio spectra of their lobes due to ageing. Other examples of such galaxies with a prominent central (kpc) emission and extended (much lower surface brightness) emission include Centaurus A, NGC 3998 and B2 0258+35.

In Centaurus A, McKinley et al. (2018) found a uniform index of $\alpha_{2300}^{154} \sim 0.8$ spread across the lobes (see their Figure 4). They argued that particle re-acceleration due to turbulence powered by the jets of the central engine is responsible for the uniform distribution of the spectral index. Presence of large-scale channels connecting the outer lobes to the centre was confirmed by Morganti et al. (1999); McKinley et al. (2018) which supports the scenario where the turbulence in the outer lobes is being maintained by the fuelling from the centre. Brienza et al. (2018) found similar properties of the spectral index in B2 0258+35. They proposed that scenarios such as jet flow disruption or episodic activity with a short interruption could power in situ particle reacceleration and/or adiabatic compression that would prevent spectral steepening. More recently Sridhar et al. (2020), in their study of NGC 3998, also found a spectral index of $\alpha_{1400}^{147} = 0.6$ uniformly spread out over the lobes (see their Figure 4). They propose similar scenarios of sputtering activity and jet flow disruption.

Jurlin et al. (2020) found a comparable fraction of restarted and remnant radio galaxies in their sample, and suggested that activity can restart in galaxies after a short remnant phase. The discovery of the above mentioned group of galaxies is in agreement with their result. Shabala et al. (2020) also found that a model with power-law distribution of the ages of radio galaxies was able to reproduce the observed fraction of restarted and

remnant radio galaxies much better than a model with a constant age for all sources. They found that the best fit model was obtained with a higher fraction of short lived sources (<100 Myr). The discovery of the above mentioned group of galaxies and the present study of 3C 293 are in line with these conclusions. This sub-group of galaxies has also been found to be gas rich, which sometimes in combination with the presence of a merger, may play a role in providing the right condition for a fast duty cycle.

In the future, more occurrences of radio sources in similar conditions could be identified using spatially resolved spectral studies down to low frequencies combined with the information about the gas medium of the host galaxy. LOFAR would provide the low frequency information, where injection and absorption effects are relevant and help estimate the age and evolutionary stage of the galaxy. APERture Tile In Focus (Apertif) phased-array feed (PAF) system (Adams & van Leeuwen 2019) would provide the HI kinematics of the host galaxy along with the higher frequency radio continuum. WHT Enhanced Area Velocity Explorer (WEAVE; Dalton et al. 2016) would be needed to probe the ionised gas properties and estimate accurate redshifts for these galaxies. Exploiting the synergy between these instruments would allow us to search for a connection between the evolutionary stage and the gas properties of these galaxies and give new insights into their life-cycle.

6. Summary and future prospects

This is the first time that the spectral properties of 3C 293 and their spatial distribution has been explored on both large and small scales down to frequencies where the breaks become apparent. 3C 293 has long been classified as a restarted galaxy, although our detailed analysis has revealed that it is not a typical restarted galaxy with a new phase of activity embedded in diffuse emission lobes with properties of remnant plasma. We find the following:

1. We have observed for the first time, absorption in the inner lobes of 3C 293 with a peak frequency of ~230-240 MHz. Free-free absorption from the NLR in the rich surrounding medium of the host galaxy is likely the dominant absorption mechanism.
2. From the age, size and presence of a turnover in the spectrum of the inner lobes of 3C 293, we conclude that they are a young CSS source whose growth is affected by the dense surrounding medium. This confirms that 3C 293 is indeed a restarted galaxy. The spectral ages of $\lesssim 0.15$ Myr & $\lesssim 0.17$ Myr represent the permanence time of the electrons in the bright compact jet components.
3. The diffuse emission seen in the centre of 3C 293 is likely formed by the leakage of radio plasma from the jet that is deflected and decelerated by interaction with the galaxy's medium.
4. The spectral properties of the outer lobes are a result of either one or maybe both of the two scenarios - multiple episodes of jet activity and turbulent jet flow due to disruption by strong jet-ISM interaction. Any interruption of jet activity has happened only a few Myr ago and the lobes are not made of remnant plasma, they are still alive. Shock powered turbulence has kept the spectra from steepening and the spectral distribution uniform. Overall, also considering the young CSS source in the centre, we conclude that 3C293 has had at least two to three epochs of activity.

Although 3C 293 has outer lobes that show spectral properties of active fuelling (and are hence alive), the presence of a young CSS source in the centre has confirmed that it is indeed a restarted galaxy. Finding similar sources and correctly categorising them separately from typical restarted galaxies is important, since shorter interruption time periods would affect the overall understanding of AGN life cycle timescales, which is a crucial input for AGN feedback models.

The ability to spatially resolve the spectral properties of the small and large-scale emission down to low frequencies can be of great importance, as shown by our study, in understanding the evolution of the radio AGN over its various life cycles and can reveal multiple epochs of activity, that single frequency morphology studies cannot do. Although resolved studies of absorption have been carried out before, they were only possible for sources with spectral peaks at GHz frequencies, due to the previously limited resolving power of instruments before the ILT. With the International stations of ILT providing sub-arcsecond resolution at 144 MHz (HBA), and in the future 57 MHz (LBA), we can now perform detailed studies of low frequency peaked sources and understand the different mechanisms that play out. Studying the ILT statistics of radio luminosity along the jets of the huge number of radio galaxies and quasars could also provide a unique diagnostic of the timeline of nuclear activity in long-living radio-loud active galaxies and quasars. This study has shown that it is crucial to quantify and probe properties at both large and small scales in order to gain a complete understanding of the different types of restarted galaxies. This opens up a new and exciting low frequency window into understanding galaxies that have eluded us at higher frequencies.

References

Adams, E. A. & van Leeuwen, J. 2019, Nature Astronomy, 3, 188
Akujor, C. E., Leahy, J. P., Garrington, S. T., et al. 1996, Monthly Notices of the Royal Astronomical Society, 278, 1
Arshakian, T. G. & Longair, M. S. 2004, Monthly Notices of the Royal Astronomical Society, 351, 727
Baars, J. W. M., Genzel, R., Pauliny-Toth, I. I. K., & Witzel, A. 1977, A&A, 500, 135
Beswick, R. J., Peck, A. B., Taylor, G. B., & Giovannini, G. 2004, Monthly Notices of the Royal Astronomical Society, 352, 49
Beswick, R. J., Pedlar, A., & Holloway, A. J. 2002, Monthly Notices of the Royal Astronomical Society, 329, 620
Bicknell, G. V., Dopita, M. A., & O'Dea, C. P. O. 1997, The Astrophysical Journal, 485, 112
Bridle, A. H., Fomalont, E. B., & Cornwell, T. J. 1981, The Astronomical Journal, 86, 1294
Brienza, M., Godfrey, L., Morganti, R., et al. 2017, Astronomy and Astrophysics, 606, 98
Brienza, M., Morganti, R., Harwood, J., et al. 2020, Astronomy & Astrophysics

Brienza, M., Morganti, R., Murgia, M., et al. 2018, Astronomy & Astrophysics, 618, A45

Brocksopp, C., Kaiser, C. R., Schoenmakers, A. P., & de Bruyn, A. G. 2007, Monthly Notices of the Royal Astronomical Society, 382, 1019

Burns, J. O., Christiansen, W. A., & Hough, D. H. 1982, The Astrophysical Journal, 257, 538

Callingham, J. R., Gaensler, B. M., Ekers, R. D., et al. 2015, Astrophysical Journal, 809, 168

Capetti, A. 2000, Astronomy and Astrophysics, 362, 871

Condon, J. J., Cotton, W. D., Greisen, E. W., et al. 1998, The Astronomical Journal, 115, 1693

Croston, J. H., Hardcastle, M. J., Harris, D. E., et al. 2005, The Astrophysical Journal, 626, 733

Dalton, G., Trager, S., Abrams, D. C., et al. 2016, in Ground-based and Airborne Instrumentation for Astronomy VI, Vol. 9908 (SPIE), 99081G

de Gasperin, F., Dijkema, T. J., Drabent, A., et al. 2019, Astronomy and Astrophysics, 622, 5

de Koff, S., Best, P., Baum, S. A., et al. 2000, The Astrophysical Journal Supplement Series, 129, 33

de Vaucouleurs, G., de Vaucouleurs, A., Corwin, H. G., J., et al. 1991, S&T, 82, 621

De Vries, N., Snellen, I. A. G., Schilizzi, R. T., Mack, K.-H., & Kaiser, C. R. 2009, A&A, 498, 641

Dey, A., Schlegel, D. J., Lang, D., et al. 2019, The Astronomical Journal, 157, 168

Eilek, J. A. 2014, New Journal of Physics, 16, 045001

Emonts, B., Morganti, R., Villar-Martin, M., et al. 2016, Astronomy and Astrophysics, 596, A19

Emonts, B. H. C., Morganti, R., Tadhunter, C. N., et al. 2005, Monthly Notices of the Royal Astronomical Society, 362, 931

Evans, A. S., Mazzarella, J. M., Surace, J. A., et al. 2005, The Astrophysical Journal Supplement Series, 159, 197

Evans, A. S., Sanders, D. B., Surace, J. A., & Mazzarella, J. M. 1999, The Astrophysical Journal, 511, 730

Fanaroff, B. L. & Riley, J. M. 1974, Monthly Notices of the Royal Astronomical Society, 167, 31P

Fanti, C. 2009, Astronomische Nachrichten, 330, 120

Feigelson, E. D., Laurent-Muehleisen, S. A., Kollgaard, R. I., & Fomalont, E. B. 1995, The Astrophysical Journal, 449, L149

Floyd, D. J. E., Perlman, E., Leahy, J. P., et al. 2005, The Astrophysical Journal, 639, 23

Greisen, E. W. 2003, in Information Handling in Astronomy - Historical Vistas, Vol. 285 (Springer Netherlands), 109–125

Hardcastle, Birkinshaw, & Worrall. 1998, Monthly Notices of the Royal Astronomical Society, 294, 615

Hardcastle, M. J. 2018, Monthly Notices of the Royal Astronomical Society, 475, 2768

Hardcastle, M. J., Birkinshaw, M., Cameron, R. A., et al. 2002, The Astrophysical Journal, 581, 948

Hardcastle, M. J. & Krause, M. G. H. 2013, MNRAS, 430, 174

Harris, D. E., Moldón, J., Oonk, J. R. R., et al. 2019, The Astrophysical Journal, 873, 21

Harwood, J. J., Hardcastle, M. J., & Croston, J. H. 2015, MNRAS, 454, 3403

Harwood, J. J., Hardcastle, M. J., Croston, J. H., & Goodger, J. L. 2013, Monthly Notices of the Royal Astronomical Society, 435, 3353

Heald, G., Mckean, J., Pizzo, R., et al. 2010, in ISKAF, 57

Hota, A., Sirothia, S. K., Ohyama, Y., et al. 2011, Monthly Notices of the Royal Astronomical Society: Letters, 417, 36

Ineson, J., Croston, J. H., Hardcastle, M. J., & Mingo, B. 2017, Monthly Notices of the Royal Astronomical Society, 467, 1586

Intema, H. T., Jagannathan, P., Mooley, K. P., & Frail, D. A. 2017, The GMRT 150 MHz all-sky radio survey: First alternative data release TGSS ADR1

Intema, H. T., Van Der Tol, S., Cotton, W. D., et al. 2009, Astronomy and Astrophysics, 501, 1185

Isobe, N., Tashiro, M., Makishima, K., et al. 2002, The Astrophysical Journal, 580, L111

Jackson, N., Tagore, A., Deller, A., et al. 2016, Astronomy & Astrophysics, 595, A86

Jackson, N., Tagore, A., Deller, A., et al. 2021, Astronomy & Astrophysics, in press

Jaffe, W. J. & Perola, G. C. 1973, Astronomy and Astrophysics, 26, 423

Jamrozy, M., Konar, C., Machalski, J., & Saikia, D. J. 2007, Monthly Notices of the Royal Astronomical Society, 385, 1286

Jamrozy, M., Saikia, D. J., & Konar, C. 2009, Monthly Notices of the Royal Astronomical Society: Letters, 399

Jetha, N. N., Hardcastle, M. J., & Sakelliou, I. 2006, Monthly Notices of the Royal Astronomical Society, 368, 609

Jeyakumar, S. & Saikia, D. J. 2000, Monthly Notices of the Royal Astronomical Society, 311, 397

Jones, D. L., Wehrle, A. E., Meier, D. L., & Piner, B. G. 2000, The Astrophysical Journal, 534, 165

Jones, D. L., Wehrle, A. E., Piner, B. G., & Meier, D. L. 2001, The Astrophysical Journal, 553, 968

Joshi, S. A., Nandi, S., Saikia, D. J., Ishwara-Chandra, C. H., & Konar, C. 2011, Monthly Notices of the Royal Astronomical Society, 414, 1397

Jurlin, N., Morganti, R., Brienza, M., et al. 2020, Astronomy and Astrophysics, 638, A34

Kameno, S., Horiuchi, S., Shen, Z.-Q., et al. 2000, PASJ, 52, 209

Kameno, S., Inoue, M., Wajima, K., Shen, Z.-Q., & Sawada-Satoh, S. 2005, in ASPC, Vol. 340, 145

Kameno, S., Sawada-Satoh, S., Inoue, M., et al. 2001, PASJ, 53, 169

Kappes, A., Perucho, M., Kadler, M., et al. 2019, Astronomy and Astrophysics, 631, A49

Kardashev, N. S. 1962, Soviet Astronomy, 6, 317

Kellermann, K. I., Kellermann, & I., K. 1966, AuJPh, 19, 195

Kellermann, K. I. & Pauliny-Toth, I. I. K. 1981, Annual Review of Astronomy and Astrophysics, 19, 373

Klein, U., Mack, K. H., Gregorini, L., & Vigotti, M. 2003, Astronomy and Astrophysics, 406, 579

Konar, C., Hardcastle, M. J., Croston, J. H., & Saikia, D. J. 2009, Monthly Notices of the Royal Astronomical Society, 400, 480

Konar, C., Hardcastle, M. J., Jamrozy, M., & Croston, J. H. 2013, Monthly Notices of the Royal Astronomical Society, 430, 2137

Konar, C., Hardcastle, M. J., Jamrozy, M., Croston, J. H., & Nandi, S. 2012, Monthly Notices of the Royal Astronomical Society, 424, 1061

Kuehr, H., Witzel, A., Pauliny-Toth, I., & Nauber, U. 1981, Astronomy and Astrophysics Supplement Series, 45, 367

Kuncic, Z., Bicknell, G. V., & Dopita, M. A. 1997, The Astrophysical Journal, 495, L35

Kuźmicz, A., Jamrozy, M., Kozieł-Wierzbowska, D., & Wezgowiec, M. 2017, Monthly Notices of the Royal Astronomical Society, 471, 3806

Labiano, A., García-Burillo, S., Combes, F., et al. 2014, Astronomy and Astrophysics, 564

Laing, R. A. & Peacock, J. A. 1980, Monthly Notices of the Royal Astronomical Society, 190, 903

Lanz, L., Ogle, P. M., Evans, D., et al. 2015, Astrophysical Journal, 801, 17

Machalski, J., Jamrozy, M., Stawarz, L., & Wezgowiec, M. 2016, Astronomy and Astrophysics, 595, 46

Mahatma, V. H., Hardcastle, M. J., Croston, J. H., et al. 2020, Monthly Notices of the Royal Astronomical Society, 491, 5015

Mahatma, V. H., Hardcastle, M. J., Williams, W. L., et al. 2018, Monthly Notices of the Royal Astronomical Society, 475, 4557

Mahony, E. K., Morganti, R., Emonts, B. H., Oosterloo, T. A., & Tadhunter, C. 2013, Monthly Notices of the Royal Astronomical Society: Letters, 435, 58

Mahony, E. K., Oonk, J. B., Morganti, R., et al. 2016, Monthly Notices of the Royal Astronomical Society, 455, 2453

Marecki, A. 2021, Astronomy and Astrophysics, 649, 6

Marecki, A., Jamrozy, M., Machalski, J., & Pajdosz-Smierciak, U. 2020, Monthly Notices of the Royal Astronomical Society, 501, 853

Martel, A. R., Baum, S. A., Sparks, W. B., et al. 1999, The Astrophysical Journal Supplement Series, 122, 81

Massaro, F., Harris, D. E., Tremblay, G. R., et al. 2010, Astrophysical Journal, 714, 589

McKinley, B., Briggs, F., Gaensler, B. M., et al. 2013, Monthly Notices of the Royal Astronomical Society, 436, 1286

McKinley, B., Tingay, S. J., Carretti, E., et al. 2018, Monthly Notices of the Royal Astronomical Society, 474, 4056

McMullin, J. P., Waters, B., Schiebel, D., Young, W., & Golap, K. 2007, ASPC, 376, 127

Mingo, B., Hardcastle, M. J., Ineson, J., et al. 2017, Monthly Notices of the Royal Astronomical Society, 470, 2762

Mohan, N., Rafferty, D., Mohan, N., & Rafferty, D. 2015, ascl, ascl:1502.007

Moldón, J., Deller, A. T., Wucknitz, O., et al. 2014, Astronomy and Astrophysics, 574, 73

Morabito, L. K., Deller, A. T., Röttgering, H., et al. 2016, Monthly Notices of the Royal Astronomical Society, 461, 2676

Morabito, L. K., Jackson, N., Mooney, S., et al. 2021, Astronomy & Astrophysics, in press

Morganti, R. 2017, Nature Astronomy, 1, 596

Morganti, R., Killeen, N. E., Ekers, R. D., & Oosterloo, T. A. 1999, Monthly Notices of the Royal Astronomical Society, 307, 750

Morganti, R., Oosterloo, T., Brienza, M., et al. 2020, Astronomy & Astrophysics

Morganti, R., Oosterloo, T. A., Emonts, B. H. C., van der Hulst, J. M., & Tadhunter, C. N. 2003, The Astrophysical Journal, 593, L69

Mukherjee, D., Bicknell, G. V., Wagner, A. Y., Sutherland, R. S., & Silk, J. 2018, Monthly Notices of the Royal Astronomical Society, 479, 5544

Murgia, M., Fanti, C., Fanti, R., et al. 2002, New Astronomy Reviews, 46, 307

Murgia, M., Parma, P., Mack, K. H., et al. 2010, Astronomy and Astrophysics, 526, 148

Murgia, M., Parma, P., Mack, K. H., et al. 2011, Astronomy and Astrophysics, 526, 148

Nandi, S., Pirya, A., Pal, S., et al. 2010, Monthly Notices of the Royal Astronomical Society, 404, 433

Nandi, S., Saikia, D. J., Roy, R., et al. 2019, Monthly Notices of the Royal Astronomical Society, 486, 5158

O'Dea, C. 1998, Publications of the Astronomical Society of the Pacific, 110, 493

O'Dea, C. P. & Baum, S. A. 1997, The Astronomical Journal, 113, 148

Offringa, A. R., de Bruyn, A. G., Biehl, M., et al. 2010, Monthly Notices of the Royal Astronomical Society, 405, 155

Offringa, A. R., McKinley, B., Hurley-Walker, N., et al. 2014, Monthly Notices of the Royal Astronomical Society, 444, 606

Offringa, A. R. & Smirnov, O. 2017, Monthly Notices of the Royal Astronomical Society, 471, 301

Offringa, A. R., Van De Gronde, J. J., & Roerdink, J. B. 2012, Astronomy and Astrophysics, 539, 95

Ogle, P., Boulanger, F., Guillard, P., et al. 2010, ApJ, 724, 1193

Orienti, M. & Dallacasa, D. 2008, Astronomy and Astrophysics, 487, 885

Orru, E., Van Velzen, S., Pizzo, R. F., et al. 2015, Astronomy and Astrophysics, 584, 112

O'Dea, C. P. & Saikia, D. J. 2021, Astronomy and Astrophysics Review, 29, 3

Parma, P., Murgia, M., De Ruiter, H. R., et al. 2007, A&A, 470, 875

Parma, P., Murgia, M., Morganti, R., et al. 1999, Astronomy and Astrophysics, 344, 7

Perley, R. A. & Butler, B. J. 2013, Astrophysical Journal, Supplement Series, 204, 19

Quici, B., Hurley-Walker, N., Seymour, N., et al. 2021, Publications of the Astronomical Society of Australia, 38

Ramírez-Olivencia, N., Varenius, E., Pérez-Torres, M., et al. 2018, Astronomy and Astrophysics, 610, 18

Roettiger, K., Burns, J. O., Clarke, D. A., & Christiansen, W. A. 1994, The Astrophysical Journal, 421, L23

Roger, R. S., Costain, C. H., & Bridle, A. H. 1973, The Astronomical Journal, 78, 1030

Saikia, D. J. & Jamrozy, M. 2009, Bulletin of the Astronomical Society of India, 37, 63

Saripalli, L., Subrahmanyan, R., Thorat, K., et al. 2012, Astrophysical Journal, Supplement Series, 199, 27

Scaife, A. M. & Heald, G. H. 2012, Monthly Notices of the Royal Astronomical Society: Letters, 423, L30

Schoenmakers, A. P., De Bruyn, A. G., Röttgering, H. J., Van Der Laan, H., & Kaiser, C. R. 2000, Monthly Notices of the Royal Astronomical Society, 315, 371

Schoenmakers, A. P., Mack, K. H., Lara, L., et al. 1998, Astronomy and Astrophysics, 336, 455

Schulz, R., Morganti, R., Nyland, K., et al. 2021, Astronomy and Astrophysics, 647, A63

Sebastian, B., Ishwara-Chandra, C. H., Joshi, R., & Wadadekar, Y. 2018, Monthly Notices of the Royal Astronomical Society, 473, 4926

Shabala, S. S., Jurlin, N., Morganti, R., et al. 2020, Monthly Notices of the Royal Astronomical Society, 496, 1706

Shimwell, T. W., Röttgering, H. J., Best, P. N., et al. 2017, Astronomy and Astrophysics, 598

Shimwell, T. W., Tasse, C., Hardcastle, M. J., et al. 2019, Astronomy and Astrophysics, 622, A1

Shulevski, A., Morganti, R., Oosterloo, T., & Struve, C. 2012, Astronomy and Astrophysics, 545, 91

Singh, V., Ishwara-Chandra, C. H., Kharb, P., Srivastava, S., & Janardhan, P. 2016, The Astrophysical Journal, 826, 132

Snellen, I. A. G., Schilizzi, R. T., Miley, G. K., et al. 2000, Monthly Notices of the Royal Astronomical Society, 319, 445

Sridhar, S. S., Morganti, R., Nyland, K., et al. 2020, Astronomy & Astrophysics, 634, A108

Stanghellini, C., O'Dea, C. P., Dallacasa, D., et al. 2005, Astronomy and Astrophysics, 443, 891

Sudou, H., Taniguchi, Y., Kaburaki, O., et al. 2001, IAUS, 205, 144

Tamhane, P., Wadadekar, Y., Basu, A., et al. 2015, Monthly Notices of the Royal Astronomical Society, 453, 2438

Tasse, C., Shimwell, T., Hardcastle, M. J., et al. 2020, Astronomy and Astrophysics, 648, A1

Tingay, S. J. & de Kool, M. 2003, The Astronomical Journal, 126, 723

Tribble, P. C. 1993, Monthly Notices of the Royal Astronomical Society, 261, 57

Turner, R. J., Shabala, S. S., & Krause, M. G. H. 2017, Monthly Notices of the Royal Astronomical Society, 474, 3361

van Breugel, W., Heckman, T., Butcher, H., & Miley, G. 1984, The Astrophysical Journal, 277, 82

van Haarlem, M. P., Wise, M. W., Gunst, A. W., et al. 2013, Astronomy and Astrophysics, 556, A2

van Weeren, R. J., Shimwell, T. W., Botteon, A., et al. 2020, arXiv, 2011.02387

van Weeren, R. J., Williams, W. L., Hardcastle, M. J., et al. 2016, The Astrophysical Journal Supplement Series, 223, 2

Varenius, E., Conway, J. E., Martí-Vidal, I., et al. 2016, Astronomy and Astrophysics, 593, 86

Varenius, E., Conway, J. E., Martí-Vidal, I., et al. 2015, Astronomy and Astrophysics, 574, 114

Vermeulen, R. C., Readhead, A. C. S., Backer, D. C., et al. 1994, Evidence for a Counter-Jet in 3C84, Tech. rep.

Walker, R. C., Dhawan, V., Romney, J. D., Kellermann, K. I., & Vermeulen, R. C. 1999, The Astrophysical Journal, 530, 233

Walker, R. C., Romney, J. D., Benson, J. M., et al. 1994, A New Feature on the Counterjet Side in 3C84, Tech. rep.

Williams, W. L., Van Weeren, R. J., Röttgering, H. J., et al. 2016, Monthly Notices of the Royal Astronomical Society, 460, 2385

Worrall, D. M. & Birkinshaw, M. 2006, Lecture Notes in Physics, 693, 39